

RESEARCH ARTICLE

10.1029/2018JA025505

EMIC Wave Events During the Four GEM QARBM Challenge Intervals

Key Points:

- EMIC waves can rapidly deplete fluxes of ultrarelativistic electrons, but their occurrences are limited in both space and time
- EMIC wave observations by magnetospheric spacecraft are supplemented by observations from ground-based magnetometers and POES satellites
- Many but not all EMIC wave events correlated with major or minor depletions of ultrarelativistic electrons observed by the Van Allen Probes

M. J. Engebretson¹, J. L. Posch¹, D. J. Braun¹, W. Li², Q. Ma^{3,2}, A. C. Kellerman³, C.-L. Huang⁴, S. G. Kanekal⁵, C. A. Kletzing⁶, J. R. Wygant⁷, H. E. Spence⁴, D. N. Baker⁸, J. F. Fennell⁹, V. Angelopoulos³, H. J. Singer¹⁰, M. R. Lessard⁴, R. B. Horne¹¹, T. Raita¹², K. Shiokawa¹³, R. Rakhmatulin¹⁴, E. Dmitriev¹⁵, and E. Ermakova¹⁶

¹Department of Physics, Augsburg University, Minneapolis, MN, USA, ²Center for Space Physics, Boston University, Boston, MA, USA, ³Department of Atmospheric and Oceanic Sciences, University of California, Los Angeles, CA, USA, ⁴Institute for the Study of the Earth, Oceans, and Space, University of New Hampshire, Durham, NH, USA, ⁵NASA/Goddard Space Flight Center, Greenbelt, MD, USA, ⁶Department of Physics and Astronomy, University of Iowa, Iowa City, IA, USA, ⁷School of Physics and Astronomy, University of Minnesota, Minneapolis, MN, USA, ⁸Laboratory for Atmospheric and Space Physics, University of Colorado Boulder, Boulder, CO, USA, ⁹The Aerospace Corporation, Los Angeles, CA, USA, ¹⁰NOAA Space Weather Prediction Center, Boulder, CO, USA, ¹¹British Antarctic Survey, Cambridge, UK, ¹²Sodankylä Geophysical Observatory, Sodankylä, Finland, ¹³Institute for Space-Earth Environmental Research, Nagoya University, Nagoya, Japan, ¹⁴Institute of Solar-Terrestrial Physics, Irkutsk, Russia, ¹⁵Borok Geophysical Observatory, Borok, Russia, ¹⁶Radiophysical Research Institute, Lobachevsky State University, Nizhny Novgorod, Russia

Supporting Information:

- Supporting Information S1

Correspondence to:

M. J. Engebretson, engebret@augsbu.edu

Citation:

Engebretson, M. J., Posch, J. L., Braun, D. J., Li, W., Ma, Q., Kellerman, A. C., et al. (2018). EMIC wave events during the four GEM QARBM challenge intervals. *Journal of Geophysical Research: Space Physics*, 123, 6394–6423. <https://doi.org/10.1029/2018JA025505>

Received 23 MAR 2018

Accepted 9 JUL 2018

Accepted article online 15 JUL 2018

Published online 16 AUG 2018

Abstract This paper presents observations of electromagnetic ion cyclotron (EMIC) waves from multiple data sources during the four Geospace Environment Modeling challenge events in 2013 selected by the Geospace Environment Modeling *Quantitative Assessment of Radiation Belt Modeling* focus group: 17 and 18 March (stormtime enhancement), 31 May to 2 June (stormtime dropout), 19 and 20 September (nonstorm enhancement), and 23–25 September (nonstorm dropout). Observations include EMIC wave data from the Van Allen Probes, Geostationary Operational Environmental Satellite, and Time History of Events and Macroscale Interactions during Substorms spacecraft in the near-equatorial magnetosphere and from several arrays of ground-based search coil magnetometers worldwide, as well as localized ring current proton precipitation data from low-altitude Polar Operational Environmental Satellite spacecraft. Each of these data sets provides only limited spatial coverage, but their combination shows consistent occurrence patterns and reveals some events that would not be identified as significant using near-equatorial spacecraft alone. Relativistic and ultrarelativistic electron flux observations, phase space density data, and pitch angle distributions based on data from the Relativistic Electron-Proton Telescope and Magnetic Electron Ion Spectrometer instruments on the Van Allen Probes during these events show two cases during which EMIC waves are likely to have played an important role in causing major flux dropouts of ultrarelativistic electrons, particularly near $L^* \sim 4.0$. In three other cases, identifiable smaller and more short-lived dropouts appeared, and in five other cases, these waves evidently had little or no effect.

1. Introduction

Many recent studies have provided increasingly detailed evidence that electromagnetic ion cyclotron (EMIC) waves are one of several mechanisms that can efficiently deplete the more energetic components of Earth's outer radiation belt (Engebretson et al., 2015; Shprits et al., 2016; Usanova et al., 2014; Xiang et al., 2017; X.-J. Zhang, Tu et al., 2016). However, occurrences of EMIC waves are limited both in space and in time. Anderson et al. (1992) found that their occurrence rate versus L shell and magnetic local time (MLT) ranged from ~10% near local noon between $L = 8$ and 9 (the apogee of the Active Magnetospheric Particle Tracer Explorers/Charge Composition Explorer spacecraft) to values of 1% or lower below $L = 6$. Usanova et al. (2012), using Time History of Events and Macroscale Interactions during Substorms (THEMIS) data, found similar occurrence rates of 2% or lower at most locations within geosynchronous orbit (6.6 R_E). Engebretson, Posch, et al. (2008) found, using data from the three Space Technology 5 spacecraft in a dawn-dusk, sun-synchronous orbit, that Pc1 wave activity was localized to rather narrow L shells (most with $\Delta L < 0.1$ or 0.2), consistent with earlier low-altitude spacecraft observations by Iyemori and Hayashi (1989) using Magsat data and by Erlandson et al. (1990) using Viking data.

Spatial coverage of EMIC waves in the region of the Van Allen radiation belts continues to be limited: Geosynchronous spacecraft are at fixed R and longitude; elliptically orbiting spacecraft cover only a small (and changing) fraction of MLT- L shell space and have a limited few-year lifetime, and there are still very few ground-based magnetometers capable of observing EMIC waves at radiation belt latitudes.

Most radiation belt simulations have had to parameterize EMIC occurrence, intensity, and (fractional) spatial coverage as the relativistic electrons drift in azimuth (Ni et al., 2015); only a few recently developed models have included MLT parameterization (e.g., the Radiation Belt Environment model, Fok et al., 2011; the British Antarctic Survey Radiation Belt Model, Glauert et al., 2014; and the Versatile Electron Radiation Belt-4D code, Shprits et al., 2015). For the four intervals selected for the Geospace Environment Modeling (GEM) Quantitative Assessment of Radiation Belt Modeling (QARBM) challenge, an attempt was made to more directly use observations. Two of these intervals included enhancements of radiation belt fluxes: a stormtime interval (17 and 18 March 2013) and a nonstormtime interval (19 and 20 September 2013). The two other intervals included flux dropouts: a stormtime interval (31 May to 2 June 2013) and a nonstormtime interval (23–25 September 2013). The data presented here extended 1 day beyond the end of the challenge interval in each case, for historical reasons. Many early ground-based studies of EMIC waves (reviewed in Engebretson et al., 2002; Engebretson, Lessard et al., 2008) reported that EMIC waves occurred most often during the middle and late recovery phases of magnetic storms. Indeed, during three of the four GEM QARBM challenge intervals, EMIC wave occurrence continued, or was even more frequent, during this additional day.

The purpose of this paper is to present a more comprehensive set of observations of EMIC waves from ground and space to help determine the role of EMIC waves in radiation belt dynamics for these events. Section 2 introduces the sources of the EMIC wave data, and section 3 presents examples of graphical summaries of the data in three different formats. Section 4 gives a detailed discussion of the observations during each of the four QARBM events, based on a graphical summary in the third format, and also compares them to simultaneous observations of relativistic and ultrarelativistic electron fluxes, phase space densities, and pitch angle distributions. Section 5 presents observations of the normalized frequencies of EMIC waves observed by the Van Allen Probes during these events, and sections 6 and 7 present a discussion of these observations and comparisons and concluding remarks.

2. Data Sources

In situ observations of EMIC waves during these four intervals were recorded by the Electric and Magnetic Field Instrument Suite and Integrated Science (EMFISIS) instrument package (Kletzing et al., 2013) on Van Allen Probes A and B (Mauk et al., 2013), which are in near-equatorial elliptical orbits with apogee at 5.9 R_E and inclination of 10° with respect to the geographic equator, and also by the vector fluxgate magnetometers on the Geostationary Operational Environmental Satellite (GOES) 13 and 15 spacecraft at geosynchronous orbit at $L = 6.8$ and 6.6 , respectively (Singer et al., 1996) and by the Fluxgate Magnetometer instrument (Angelopoulos, 2008) on THEMIS D and E, in elliptical orbits with apogee at 12–13 R_E (http://themis.ssl.berkeley.edu/orbits_more.shtml) and inclination of 5 – 12° with respect to the geographic equator. Although these spacecraft observed EMIC waves at or near the location of their generation, their orbits, with periods ranging from 6 to 24 hr, cover only a small fraction of MLT- L shell space at any one time. Because these are local measurements and because many EMIC waves are generated in narrow regions of L and MLT, a wave occurring $>0.5 R_E$ radially away from the spacecraft is likely to not be observed. Also shown from the Van Allen Probes are plasma density data obtained by the Electric Fields and Waves (EFW) instrument (Wygant et al., 2013) and radiation belt electron flux data obtained by the Relativistic Electron-Proton Telescope (REPT) instrument (Baker et al., 2013) and the Magnetic Electron Ion Spectrometer (MagEIS) instrument (Blake et al., 2013), both part of the Energetic Particle, Composition, and Thermal plasma suite (Spence et al., 2013). More information on these instruments is provided in Engebretson et al. (2015) and Tetrick et al. (2017).

In order to provide optimal data coverage from ground-based magnetic field sensors, we accessed digital data and/or daily frequency versus time spectrograms from several arrays of search coil (induction) magnetometers as well as single-stations worldwide with sufficiently high sampling rates (at least 5 Hz) and within the L range of the radiation belts ($L = 2$ to 7). If wave spectrograms were not already publicly available,

Table 1
Ground-Based Induction Coil Arrays and Stations Used in This Study

	Geog. lat.	Geog. lon.	CGM lat.	CGM lon.	L shell
CARISMA					
Dawson	64.05	220.89	65.96	275.20	6.12
Fort Smith	60.02	248.05	67.15	308.18	6.74
Ministik Lake	53.35	247.03	60.49	309.06	4.19
Fort Churchill	58.76	265.92	68.04	334.64	7.27
Pinawa	50.20	263.96	59.74	332.72	4.00
Thief River Falls	48.03	263.64	57.59	332.45	3.54
Finnish Chain					
Kilpisjärvi	69.02	20.86	66.09	103.04	6.18
Ivalo	68.55	27.28	65.36	107.92	5.84
Sodankylä	67.42	26.39	64.24	106.50	5.38
Rovaniemi	66.78	25.94	63.60	105.76	5.14
Oulu	65.08	25.90	61.85	104.85	4.56
Nurmijärvi	60.51	24.65	57.10	101.86	3.44
Antarctica					
Halley	−75.60	−26.30	−62.30	29.93	4.70
South Pole	−90.00	—	−83.62	170.25	~13
STEL					
Magadan	60.05	150.73	54.26	220.41	2.98
Paratunka	52.97	158.25	46.78	227.77	2.17
Moshiri	44.37	142.27	37.91	214.80	1.63
Athabasca	54.60	246.36	61.42	306.59	4.44
Russian stations					
Borok	58.07	38.23	54.43	113.18	3.00
Nizhny Novgorod	56.30	43.94	52.63	118.11	2.76
Uzur	51.25	100.99	46.97	174.76	2.18

Note. Array names are given in bold lettering. The dash (—) indicates that South Pole has an undefined longitude value. Corrected geomagnetic (CGM) coordinates calculated using VITMO ModelWeb, https://omniweb.gsfc.nasa.gov/vitmo/cgm_vitmo.html, for epoch 2013. CARISMA = Canadian Array for Realtime Investigations of Magnetic Activity; Solar-Terrestrial Environment Laboratory.

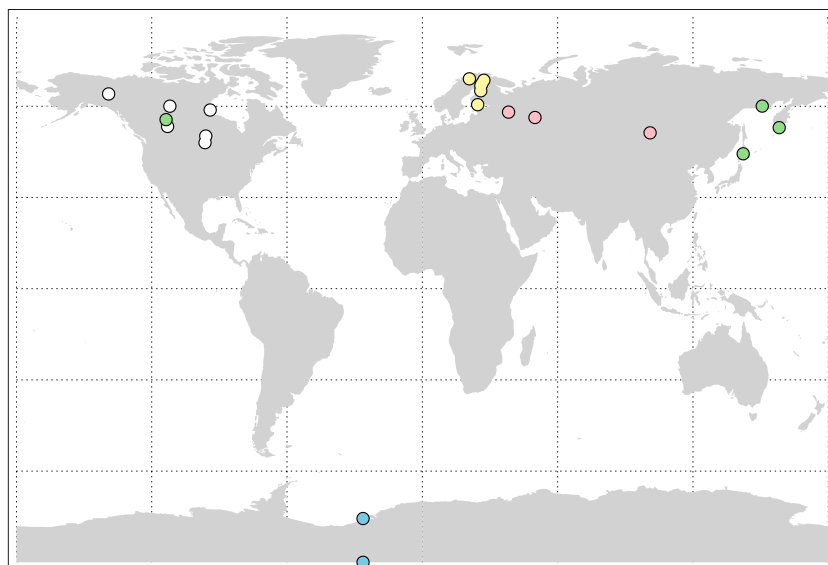


Figure 1. Map showing the geographical location of the induction coil magnetometers used in this study, color coded as follows: Canadian Array for Realtime Investigations of Magnetic Activity stations in white, Finnish chain stations in yellow, Russian stations in pink, STEL array stations in green, and Antarctic stations in blue.

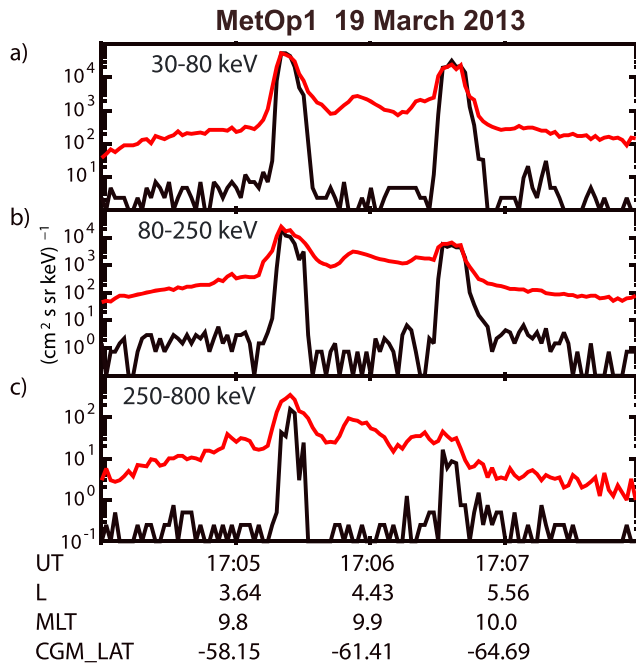


Figure 2. Count rates from the 90° proton detectors (red, trapped) and the 0° (black, in the loss cone), respectively, in the 30–80-, 80–250-, and 250–800-keV proton channels of the MetOp 1 satellite, from 17:04 to 17:08 UT 19 March 2013. UT = universal time; MetOp = Meteorological OPERational; MLT = magnetic local time.

digital data were acquired at the maximum native resolution of these magnetometers and daily 0–1 and 0–5 Hz Fourier spectrograms were produced. Table 1 lists the arrays and stations accessed, and Figure 1 is a map showing their geographical distribution.

EMIC waves propagate along magnetic field lines from the location of their origin toward both northern and southern ionospheres (Horne & Thorne, 1993). When they impinge on the ionosphere, however, a significant fraction of their energy is ducted horizontally, that is, converted into fast mode waves that can travel horizontally in the F-region waveguide (Fraser, 1975; Fujita & Tamao, 1988; Greifinger & Greifinger, 1968; Kim et al., 2010, 2011) before emerging below the ionosphere as electromagnetic waves. These waves are then detected by magnetometers on the ground, with locations ranging from immediately below the flux tube on which the wave was generated to distances of up to 2,000 km (Kim et al., 2010). Propagation is predicted to be more efficient, however, along the magnetic meridian than out of the meridian plane (Fujita, 1988; Greifinger & Greifinger, 1973). Ground-based induction magnetometers can thus take advantage of ionospheric ducting to observe waves that originate over a fairly wide range of latitudes, but as a result a single magnetometer can provide little or no information about the *L* shell on which the waves originated, and its measured amplitude cannot be used to accurately infer the amplitude of those waves in space. As Figure 1 indicates, there are large ranges of longitude with little coverage, and only at three longitudes are there enough stations to help localize the *L* shell based on its relative amplitude. Even though each array or station passes through a specific MLT region only once per day, these arrays and stations provide much wider spatial and

temporal coverage than the necessarily local observations made by spacecraft in the near-equatorial magnetosphere.

A third source of information about EMIC wave activity comes from observations of precipitating ring current protons by the six low-altitude orbiting sun-synchronous Polar Operational Environmental Satellite (POES) spacecraft in operation during 2013: National Oceanic and Atmospheric Administration (NOAA) POES 15, 16, 18, and 19 and Meteorological OPERational (MetOP) 1 and 2.

Several studies have provided evidence of the link between EMIC wave activity and proton precipitation peaks in the 30–80, 80–250, and 250–800 keV proton channels of the Medium Energy Proton and Electron Detector (Evans & Greer, 2004) instrument mounted on each of these spacecraft: Lundblad and Soraas (1978), Søråas et al. (1980), Yahnina et al. (2000), Sandanger et al. (2007), Yahnin and Yahnina (2007), and Carson et al. (2013). Most recently, Summers et al. (2017) used POES data such as that shown in Figure 2 to infer that proton precipitation was caused by EMIC waves and that EMIC wave action was prevalent at the times and *L*-shell locations of the most intense proton spectra observed by the Radiation Belt Storm Probes Ion Composition Experiment instrument on the Van Allen Probes. Figure 2 was selected for two reasons: First, it demonstrates the typical (but not universal) narrow width in *L* of EMIC wave events. The first precipitation event peaked in the 30–80 keV channel at 17:05:21 universal time (UT), had a peak flux of 5×10^4 counts $(\text{cm}^2 \text{ s sr})^{-1}$, and reached the 100 count level at *L* shells of 3.84 and 4.03, thus having a full width at the 100 count level of 0.19 *L*. The second event peaked in the 30–80 keV channel at 17:06:36, had a peak count rate of 3×10^4 counts $(\text{cm}^2 \text{ s sr})^{-1}$, and reached the 100 count level at *L* shells of 4.93 and 5.28, thus having a full width at the 100 count level of 0.35 *L*. Second, although in most cases, POES spacecraft observe only one latitudinally narrow peak (or none) during each pass through radiation belt latitudes, two or on occasion even three narrow peaks can be observed. Both of these features indicate that EMIC waves can be very localized in *L* shell. It is not yet understood why this is the case, but it suggests that generation of EMIC waves can be sensitive to local conditions. Under conditions of high solar wind pressure, EMIC waves have been observed on multiple *L* shells and across a wide range of local times (Engebretson et al., 2015).

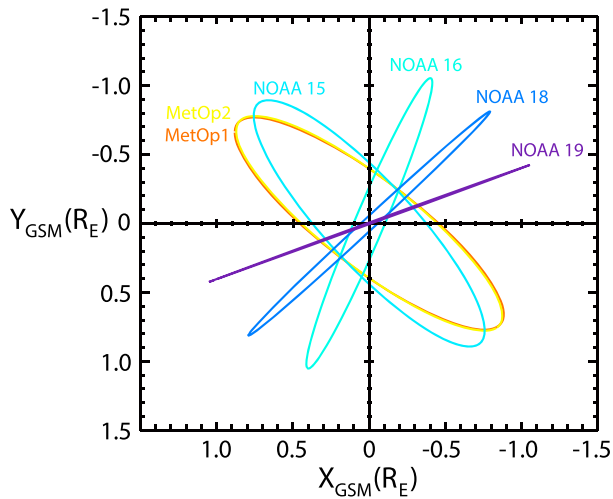


Figure 3. Orbits of MetOp 1 (orange), MetOp 2 (yellow), NOAA 15 (light blue), NOAA 16 (aqua), NOAA 18 (blue), and NOAA 19 (purple) in the GSM XY plane, from 10:00 to 11:41 universal time 19 March 2013. The Sun is to the left. MetOp = Meteorological Operational; NOAA = National Oceanic and Atmospheric Administration; GSM = geocentric solar magnetospheric.

The six POES spacecraft provide an additional complement to both magnetospheric in situ and ground-based wave observations, in that each spacecraft orbits Earth with a ~100-min period, and each measurement provides localized information on L shell. The availability of six spacecraft increases the local time coverage, but unfortunately, two are in nearly the same orbital plane, and none provides good coverage near midnight, dawn, noon, or dusk (Figure 3).

We removed all POES events occurring within the South Atlantic Magnetic Anomaly. This resulted in the removal of 12 events out of a total of 107 events, with one exception: NOAA 15 was in the South Atlantic Magnetic Anomaly near 22:34 UT on 2 June, fairly close to the time that Van Allen Probes A and B were in the same UT-MLT- L region. That event has been retained, but its amplitude and trapped to precipitating flux ratios are suspect.

3. Data Products

Data products in three different presentation formats are available for GEM challenge modelers at <https://drive.google.com/drive/folders/0ByNhSbWkAgdfNTNnMEV1LWFOc2c>. This section introduces examples of each format, and the following section presents observations in the third format as well as relativistic electron data for each of the four challenge intervals.

The most detailed presentation format consists of an L versus MLT table created for each hour UT for each day. Table 2 shows an example of this format, for 8 to 9 UT on 3 June 2013. THEMIS-E observed a 0.2-nT rms amplitude helium-band EMIC wave from 08:45 to 08:48 UT as it passed outbound from $L = 4.1$ to 4.2 near 00:25 MLT. EMIC wave activity near 0.5 Hz began at Magadan and Paratunka (part of the Solar-Terrestrial Environment Laboratory (STEL) array) near 08:00 UT, when these stations were in the 16–20 MLT sector,

but was not observed at lower latitude stations in that array. Because the STEL array reaches only to $L \sim 3$, we can only infer a lower- L boundary for this event. EMIC waves were also observed by several Canadian Array for Realtime Investigations of Magnetic Activity (CARISMA) stations (Mann et al., 2008), which were located during this hour in the 20–24 MLT sector. These waves, with frequency near 1.0 Hz, were the strongest at the two lowest latitude stations in the eastern segment of CARISMA, Pinawa and Thief River Falls. As a result, we inferred an L range from 3.5 to 4.5 for this event. NOAA 16 observed an intense precipitation event, 7×10^4 counts $(\text{cm}^2 \text{ s sr})^{-1}$, in this same UT and MLT interval, at 08:43:25 UT as the spacecraft passed from $L = 3.95$ to 4.10 near MLT = 23:00. In this example, the POES data confirm the inference of L shell location based on CARISMA magnetometer observations.

There is as yet no accepted calibration to allow conversion from POES proton precipitation count rates to wave amplitudes in the magnetosphere. EMIC waves are instead inferred as the source of localized peaks when the precipitating and trapped proton fluxes are nearly the same. Y. Zhang, Shi, et al. (2017), using the same theoretical framework used by W. Li et al. (2013) and Ni et al. (2014) to infer chorus wave amplitude from the ratio of precipitating to trapped POES electron precipitation fluxes, presented a technique that resulted in an asymptotic calibration curve for ratios near 1, corresponding to waves with amplitude 1 nT and larger. However, degradation of the Medium Energy Proton and Electron Detector telescopes on each of the POES spacecraft, documented recently by Sandanger et al. (2015) and Ødegaard

Table 2
Event Grid Example Showing Electromagnetic Ion Cyclotron Wave Activity From 8 to 9 UT on 3 June 2013

3 June 2013		8–9 UT					
		MLT					
		0–4	4–8	8–12	12–16	16–20	20–24
0–0.5							
0.5–1							
1–1.5							
1.5–2							
2–2.5						STEL	
2.5–3						STEL	
3–3.5						STEL	
3.5–4						STEL	CARIS, 1.1-nT POES
L 4–4.5	0.2-nT He THEMIS-E					STEL	CARIS, 1.1-nT POES
4.5–5						STEL	
5–5.5						STEL	
5.5–6						STEL	
6–6.5						STEL	
6.5–7							
>7							

Note. UT = universal time; MLT = magnetic local time; CARIS = Canadian Array for Realtime Investigations; THEMIS = Time History of Events and Macroscale Interactions during Substorms; POES = Polar Operational Environmental Satellite.

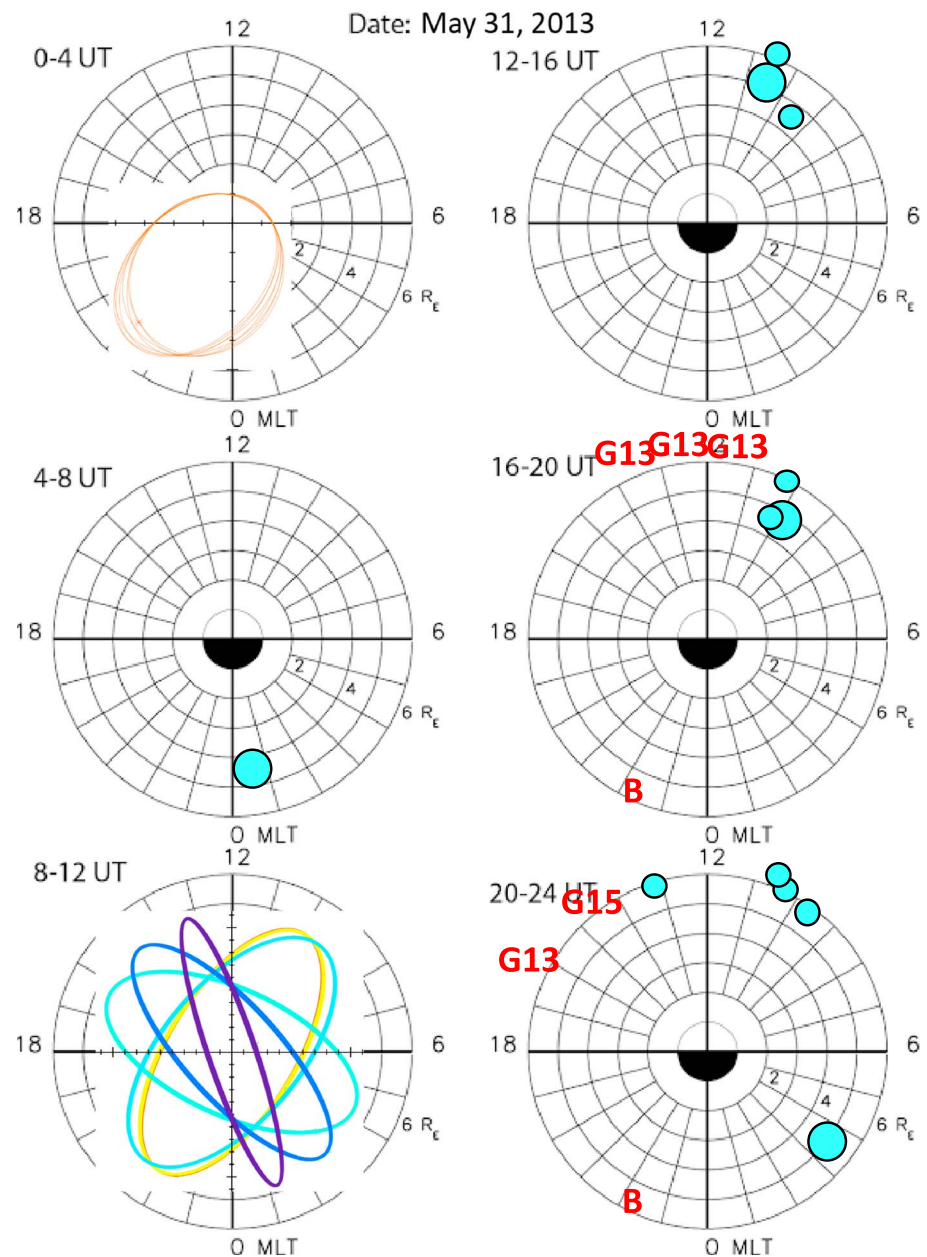


Figure 4. An example daily dial plot page from 31 May 2013 showing electromagnetic ion cyclotron wave activity observed in situ by magnetospheric spacecraft (G13: Geostationary Operational Environmental Satellite 13; G15: Geostationary Operational Environmental Satellite 15; B: Van Allen Probe B) and observed indirectly as ring current proton precipitation observed by the POES spacecraft during each 4 hr of UT. The larger and smaller blue circles denote POES proton precipitation events with peak fluxes of $>10^4$ and between 10^3 and 10^4 counts $(\text{cm}^2 \text{ s sr})^{-1}$, respectively, in the 30–80 keV channel. Orbit plots of the Van Allen Probes on this day are superposed on the 0–4 UT dial, and orbit plots of the POES spacecraft (enlarged in radius, not to scale) are superposed on the 8–12 UT dial. POES = Polar Operational Environmental Satellite; UT = universal time.

et al. (2016), was not factored into the Y. Zhang et al. calibrations. Our estimate of the wave amplitude corresponding to the observed precipitating proton counts and ratios of trapped and precipitating fluxes is loosely based on the Y. Zhang, Shi, et al. (2017) calibration and should be treated with caution: any values above 0.5-nT rms given in these tables may be significantly underestimated.

The second presentation format consists of a set of six L -MLT dial plots for each day during each of the four challenge intervals, each covering 4-hr UT. An example from 31 May 2013 is shown in Figure 4. Each EMIC

wave event observed in the magnetosphere on this day by the GOES, Van Allen Probes, and THEMIS spacecraft is shown in its respective UT intervals, as are all the POES proton precipitation events, which in this format (and also the third format) are grouped according to count rates in the 30–80 keV proton channel. No wave or proton precipitation events were recorded in the 0–4 UT or 8–12 UT time intervals, and only one POES proton precipitation event, with peak flux of 1.5×10^4 counts $(\text{cm}^2 \text{ s sr})^{-1}$, was observed near 06:59 UT by MetOp 1 at 0.6 MLT and $L = 4.35$. As will be shown in Figure 10, the solar wind dynamic pressure P_{sw} was high and increasing after 14 UT. This pressure increase was reflected in a large number of dayside POES precipitation events in the three later dial plot panels. However, no POES proton precipitation events were recorded within 1-hr MLT of local noon. We believe this is a consequence of the limited MLT coverage of the POES spacecraft shown in the 8–12 UT dial. No information about ground-based observations is included in this second set of plots, but significant wave activity was observed by ground-based induction magnetometers in Finland, Antarctica, and Canada between 15 and 23 UT.

Nearly continuous intense (3-nT rms) 0.3-Hz He band EMIC waves were recorded by GOES 13 from 16:20 to 19:40 UT (11:15 to 14:55 MLT) and similarly intense 0.2-Hz He band waves from 21:00 to 22:30 UT (1617 to 1746 MLT). GOES 15 also recorded 2-nT rms 0.4-Hz He band EMIC waves from 22:40 to 23:30 UT (13:56 to 14:46 MLT).

The orbital track of Van Allen Probe B on this day has been superposed on the 0–4 UT dial plot. This spacecraft was not in position to observe any of the dayside activity recorded by the POES spacecraft or ground-based induction magnetometer arrays. Van Allen Probe B did record 1.3-nT rms 0.25-Hz He band waves from 19:32 to 19:47 UT (22:05 to 22:10 MLT, 4.9–5.1 L) and 2-nT rms 0.25-Hz He band waves from 19:58 to 20:10 UT (22:20 to 22:30 MLT, 5.4–5.6 L). Wave activity at the same frequency was recorded by the Finnish induction magnetometer array during this interval.

The third presentation format consists of one stacked multipanel plot for each challenge event, as in Figures 5a–5f. Figures 5a–5c show the solar wind dynamic pressure (P_{sw}), the 1-min AE index, and the 1-min SYM/H index, respectively. Figure 5d shows EMIC wave activity as a function of L and universal time, for 23–26 September 2013, coded by spacecraft according to the legend at the right. EMIC waves with amplitude exceeding 5-nT rms are shown in a larger font. Figure 5e shows EMIC wave observations by ground-based induction magnetometers as a function of UT and inferred L shell ranges, color-coded as in Figure 1, but conveys no amplitude or MLT information. As in Table 2, a wide range of L shells indicates large uncertainty because of limited station coverage, whereas a narrower range of L shells indicates better localization of the waves. Figure 5f shows ring current proton precipitation spikes observed by the POES spacecraft as a function of UT and L but conveys no MLT information. As in Figure 4, the legend to the right denotes the amplitude of the precipitating flux in counts $(\text{cm}^2 \text{ s sr})^{-1}$ in the 30–80-keV channel.

Data presentations such as Figures 5a–5f do not provide evidence of close conjunctions in MLT, or the lack of them, between ground-based, POES, and satellite observations. However, the very rapid longitudinal drift of relativistic electrons insures that any EMIC wave event with a duration of more than a few minutes will interact with the entire population of relativistic electrons in that same L range, so strong EMIC wave activity in that L range at any MLT may act to alter their pitch angle distributions and contribute to their losses.

Figures 5g–5j present Van Allen Probes observations of relativistic and ultrarelativistic electrons. Figure 5g shows the time dependence of the total radiation belt content (TRBEC), as defined in Boyd (2016) and Forsyth et al. (2016): the total number of electrons observed by the Van Allen Probes with first adiabatic invariant μ between 500 and 2,000 MeV/G, integrated over all pitch angles (second adiabatic invariant, K), and over all L^* values between $L^* = 2.5$ and the Van Allen Probes apogee ($5.9 R_E$). By performing this integration over each half orbit, this provides an estimate of the radiation belt content every ~ 3 hr that is interpolated onto a regular 3-hr timeline. The blue box in Figure 5g anticipates the results of our detailed analysis: It indicates the approximate time and L ranges in which EMIC-induced depletions of ultrarelativistic electrons were observed. Figures 5h–5j show spin-averaged fluxes of relativistic and ultrarelativistic electrons measured by the REPT instrument on Van Allen Probes A and B in L versus time format in three energy channels: 2.6, 4.2, and 5.2 MeV, respectively, as a function of L and time. The L values are based on the TS05 (Tsyganenko & Sitnov, 2005) magnetic field model for 90° pitch angles and are obtained from the Energetic Particle,

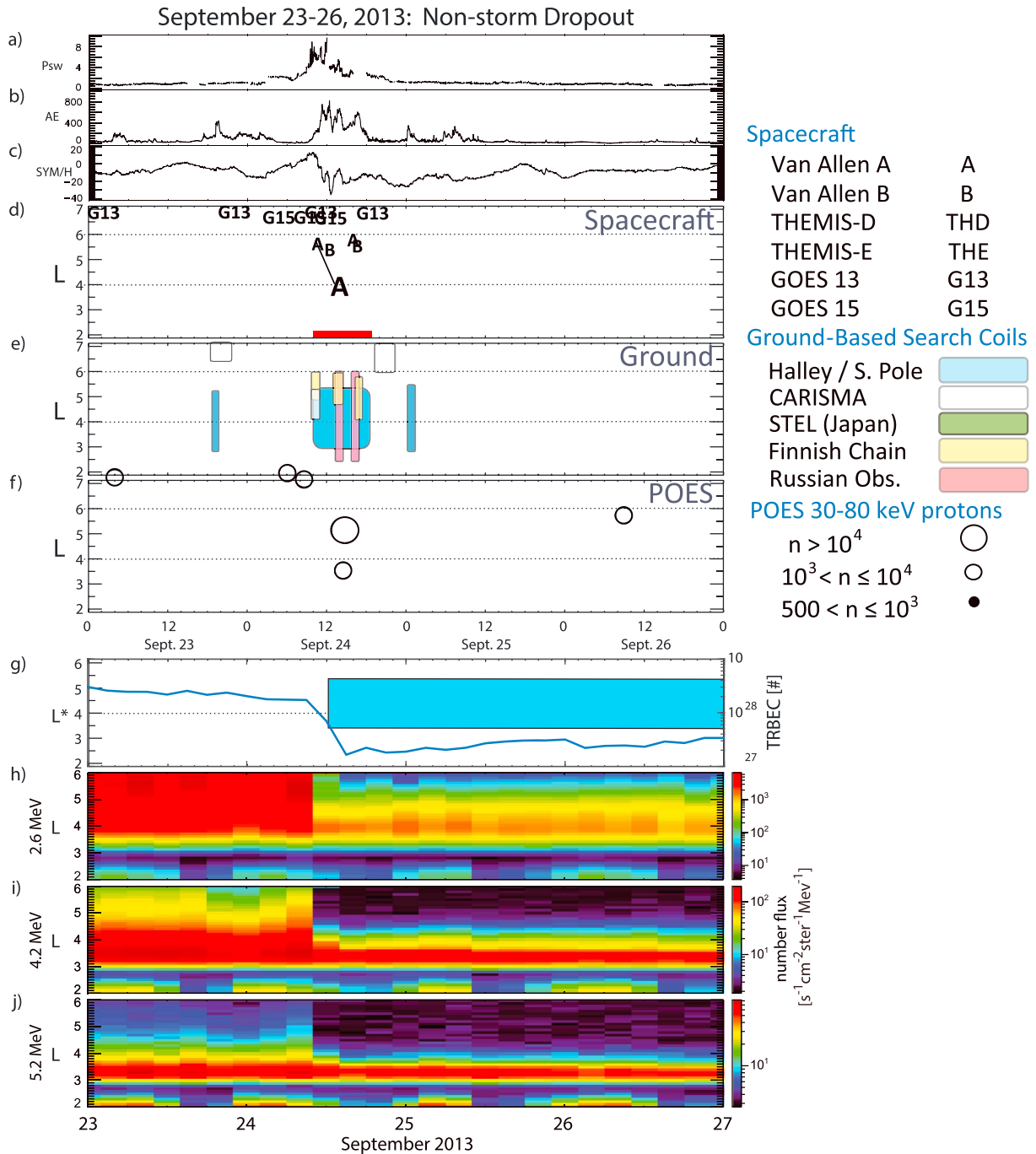


Figure 5. Nonstormtime dropout interval from 23 September through 26 September 2013. (a), (b), and (c) show the solar wind dynamic pressure (Psw), the 1-min AE index, and the 1-min SYM/H index, respectively. (d), (e), and (f) summarize EMIC wave activity as a function of L and universal time observed in situ by spacecraft magnetometers, by ground-based induction magnetometers, and by POES proton detectors, respectively, according to the legends on the right. The red bar at the bottom of (d) indicates an interval of ground-based observations of intense EMIC waves. (g) shows the total radiation belt electron content (TRBEC, scale on the right) and the blue box indicates the L^* and universal time ranges in which EMIC wave-induced depletions of ultrarelativistic electrons were observed. (h), (i), and (j) show spin-averaged differential fluxes of relativistic and ultrarelativistic electrons measured by the Relativistic Electron-Proton Telescope instrument on Van Allen Probes A and B in three energy channels: 2.6, 4.2, and 5.2 MeV. EMIC = electromagnetic ion cyclotron; POES = Polar Operational Environmental Satellite; THEMIS = Time History of Events and Macroscale Interactions during Substorms; GOES = Geostationary Operational Environmental Satellite; CARISMA = Canadian Array for Realtime Investigations of Magnetic Activity.

Composition, and Thermal Plasma magnetic ephemeris data product. Electron measurements by both Probes A and B are binned into 0.1 L shell grids and 4-hr UT intervals.

4. EMIC Events During the Challenge Intervals

In this section we discuss the EMIC wave observations obtained by the instruments described in section 2 during each of the four QARBM challenge intervals and their relation to electron fluxes observed in the radiation belts by the Van Allen Probes MagEIS and REPT instruments. For each interval, we will begin with a figure in the third format, combining EMIC wave observations in Figures 5a–5f with TRBEC data and REPT spin-averaged differential flux data in Figures 5g–5j. Following this will be phase space density plots and normalized pitch angle spectrograms for selected intervals of EMIC activity, as well as additional detailed observations of EMIC waves during two of the times when they were evidently effective in depleting the electron fluxes.

4.1. Nonstorm Dropout Interval: 23–26 September 2013

Su et al. (2016) presented observations and simulations of this interval and showed that the relativistic electron loss in the region $L = 4.5$ – 6.0 was primarily caused by pitch angle scattering by observed plasmaspheric hiss and electromagnetic ion cyclotron waves.

Figure 5a shows that P_{sw} began a gradual increase from ~ 1 to 2 nPa near 02:00 UT on the second day of this interval, 24 September, and rose sharply to over 8 nPa between 08:00 UT and 11:00 UT before gradually subsiding again. The AE index began to gradually and then sharply rise from near 50 nT at 09:00 UT to ~ 750 nT near 11:00 UT and remained above 300 nT until 17:00 UT (Figure 5b). SYM/H increased gradually from -10 nT at 02:00 UT to over 10 nT at 10:00 UT before dropping to -30 nT near 12:30 UT in a weak storm-like main phase (Figure 5c).

Figure 5d shows that wave activity at GOES 13 ($L = 6.8$) appeared near 03:30 UT and 20:00 UT on 23 September, possibly in response to the increased AE index observed near those times, and again on 24 September during intervals of large AE between 10:00 and 13:00 UT and again near 16:00 and 18:00 UT. Intense wave activity at GOES 15 ($L = 6.6$) in both the H and He bands appeared between 04:00 and 05:00 UT and wave bursts appeared at 09:00 (He band), 12:40 (H band), and 13:30 UT (H band).

As will be shown in Figure 6, strong to intense EMIC waves increasing in center frequency from ~ 0.3 to ~ 1.2 Hz were observed on 24 September by Van Allen Probe A near 20 MLT from 11:40 UT (1.2-nT rms) at $L = 5$ to 12:50 UT (16.4-nT rms) at $L = 3.9$. Probe A also observed strong ~ 0.4 -Hz He band EMIC waves (2.9-nT rms) and weaker ~ 0.65 Hz, 0.6-nT rms amplitude waves in the H band) from $L = 5$ to 5.5 near 17 MLT from 16:40 to 17:25 UT during the following outbound pass. Van Allen Probe B observed strong ~ 0.55 Hz, 2.2-nT rms amplitude waves in the He band and weaker ~ 1.0 Hz, 0.3-nT rms amplitude H band waves between 13:18 and 13:28 from $L = 4.8$ to 5.0 near 16.4 MLT. Probe B also observed ~ 0.7 Hz, 1.3-nT rms amplitude H band waves at 16:54 UT near 19 MLT and $L = 5.4$ as it began its inbound pass.

Ground-based EMIC waves (Figure 5e) appeared in CARISMA data at $L > 6$ from 18:00 to 22:00 UT (10:00–14:00 MLT) 23 September and 19:00 to 22:00 UT (11:00–14:00 MLT) 24 September, in rough temporal agreement with GOES 13 wave observations. Between 10:00 and 19:00 UT, three arrays observed EMIC wave activity: Halley observed moderate intensity 0.1–0.5-Hz wave activity from 19:00 to 20:00 UT 23 September as it moved from 15:00 to 16:00 MLT and sporadically from 10:00 to 19:00 UT as it moved from 07:00 to 15:00 MLT and a brief burst of strong rising-tone 0.1–0.6-Hz wave activity near 00:00 UT September 25, when it was near 20:00 MLT. The Finnish chain observed three bursts of strong to intense 0.1–0.4-Hz EMIC wave activity between 10:00 and 17:00 UT, with the highest amplitude at Rovaniemi and Sodankylä, at $L = 4.9$ and 5.2, respectively, and much weaker power (most likely ducted) at Nurmijärvi ($L = 3.44$). Higher frequency wave activity, the strongest between 1.2 and 2.0 Hz from 13:00 to 13:15 UT, was observed at Magadan, in eastern Siberia ($L = 2.98$, the highest-L station in the STEL array), and waves with similar temporal and frequency structure were observed at Uzur ($L = 2.18$).

Six moderate to strong POES precipitation events occurred during this interval (Figure 5f). The first three, with moderate intensity, occurred in near coincidence in time and L shell with EMIC waves observed at GOES 13 and 15. Another moderate intensity event was observed by NOAA 16 north of Irkutsk, Russia, near

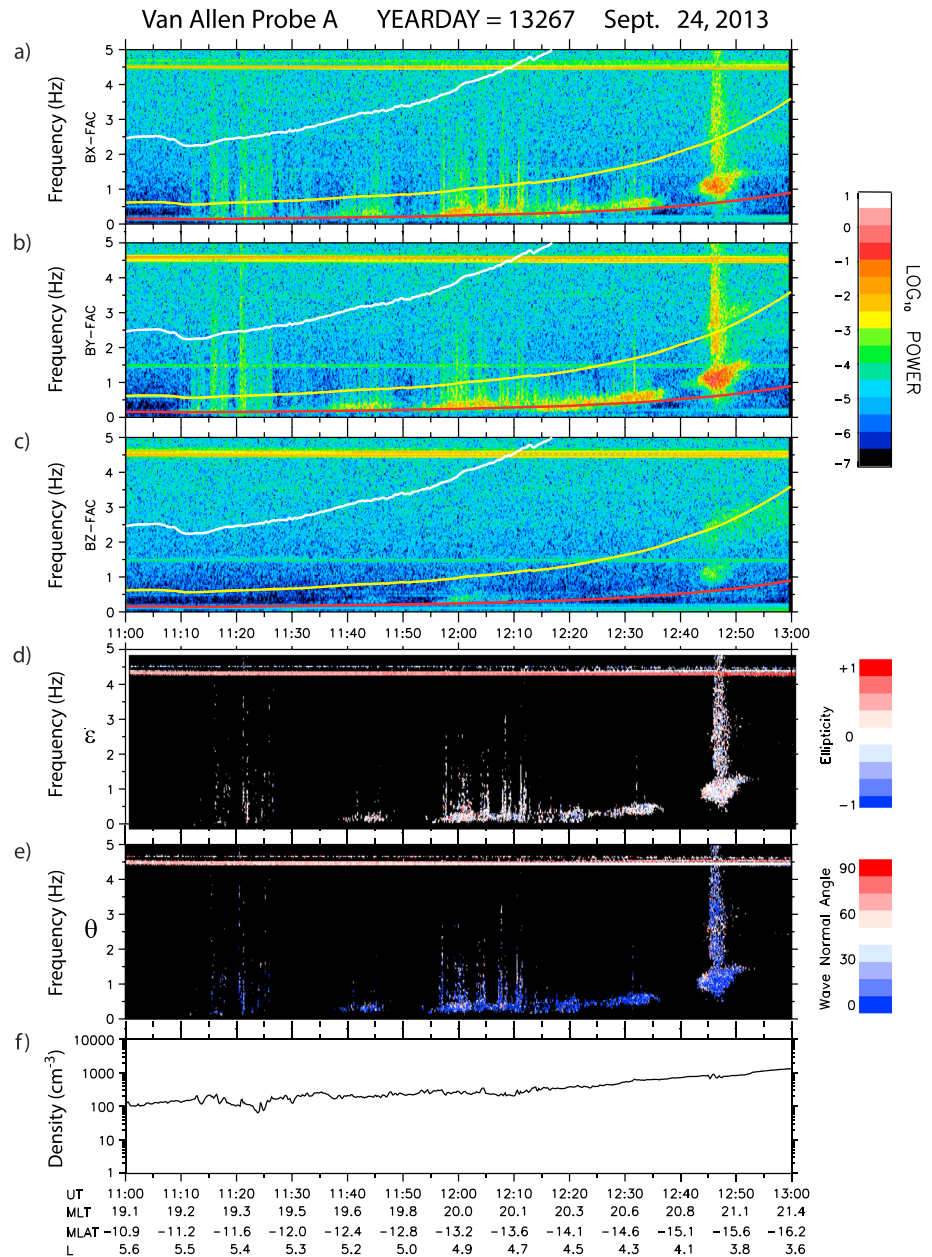


Figure 6. Van Allen Probe A Electric and Magnetic Field Instrument Suite and Integrated Science magnetic field data and Electric Fields and Waves plasma density data from 11:00 to 13:00 UT 24 September 2013. (a–c) are Fourier spectrograms of differenced magnetic field data in local field-aligned coordinates: Bx (transverse and radially outward), By (transverse eastward), and Bz (parallel to the local field), respectively. (d) and (e) are spectrograms of the ellipticity and wave normal angle, respectively, shown when the wave power exceeds $10^{-3} \text{ nT}^2\text{-Hz}$. (f) shows the plasma density obtained from the Electric Fields and Waves instrument. UT = universal time; MLT = magnetic local time; MLAT = magnetic latitude.

$L = 3.6$ at 13:13 UT, and a strong precipitation event was observed by NOAA 18 over Norway near $L = 5.2$ at 13:50 UT.

The total radiation belt electron content shown in Figure 5g dropped by nearly a factor of 10 between 09:00 and 15:00 UT on 24 September and increased only modestly during the following days. Figure 5h shows a sharp dropout in 2.6-MeV fluxes beyond $L = 3.5$ after $\sim 10:00$ UT 24 September, and similar dropouts are also evident in the 4.2- and 5.2-MeV channels (Figures 5i and 5j, respectively). Note, however, that although the

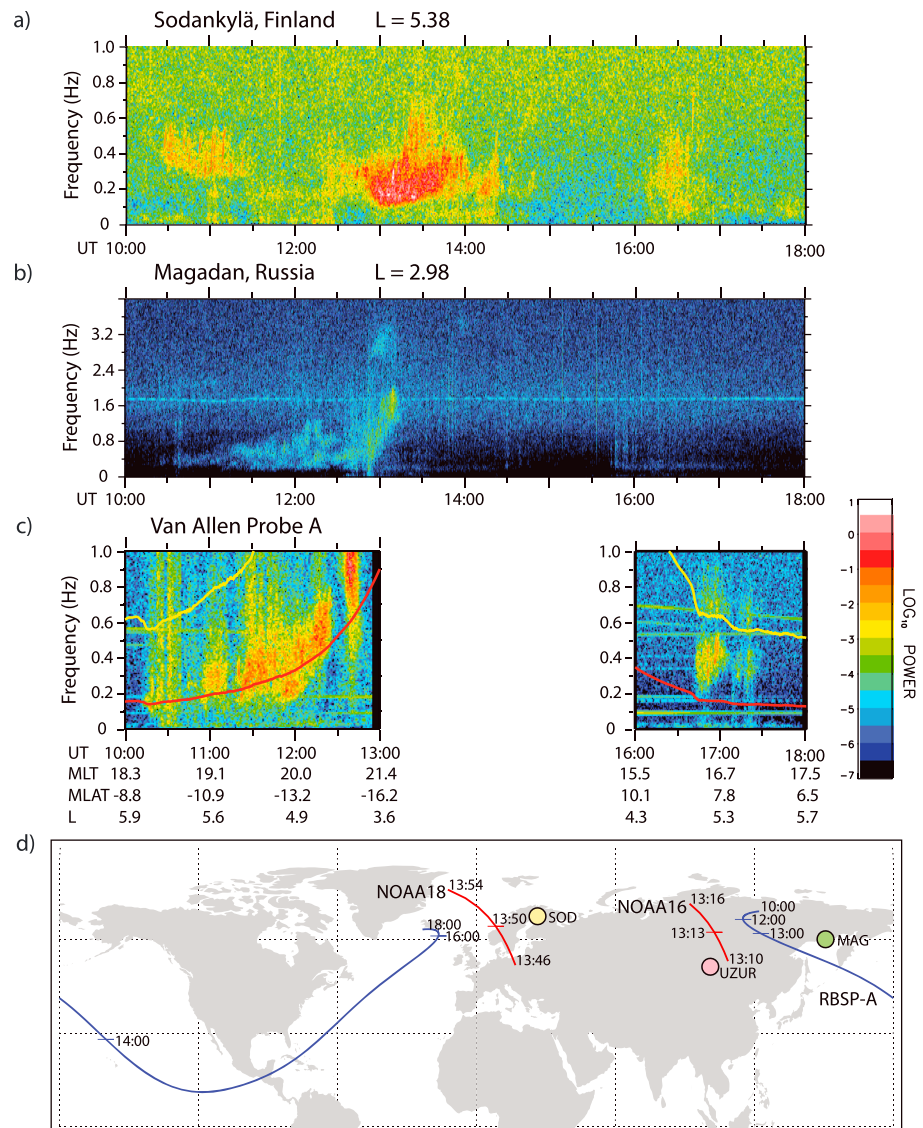


Figure 7. Composite figure showing spectrograms of the B_y (eastward) components of magnetic field data from Sodankylä, Finland (a), Magadan, Russia (b), and Van Allen Probe A (c) from 10:00 to 18:00 UT 24 September 2013 and a map (d) showing the Northern Hemisphere magnetic footprints of Van Allen Probe A from 10:00 to 18:00 UT, of NOAA 16 from 13:12 to 13:14 UT, and of NOAA 18 from 13:45 to 13:55 UT, respectively, on 24 September 2013. The locations of Magadan, Uzur, and Sodankylä are indicated by green, pink, and yellow circles, respectively. UT = universal time; MLT = magnetic local time; MLAT = magnetic latitude; NOAA = National Oceanic and Atmospheric Administration; RBSP-A = Radiation Belt Storm Probe-A (Van Allen Probe A).

fluxes in the 2.6-MeV channel remained relatively steady after 10:00 UT, fluxes in the 4.2- and 5.2-MeV channels dropped again during the following 4-hr interval. This second drop might be attributable to the EMIC waves observed between 10 and 17 UT.

Figures 6 and 7 provide more details on the EMIC events between 10:00 and 18:00 UT on 24 September. Figures 6a–6c are 0 to 5-Hz Fourier spectrograms of Van Allen Probe A EMFISIS vector magnetic field data from 1100 to 13:00 UT after rotating into local field-aligned coordinates and differencing (to whiten the spectra; Engebretson, Lessard et al., 2008; Takahashi et al., 1990). The X and Y directions are perpendicular to the local magnetic field: X is directed radially outward, and Y is directed azimuthally eastward. Wave power in nT^2/Hz is color-coded according to the color bar at the right. The local oxygen, helium, and hydrogen ion gyrofrequencies, identified from the magnitude of the observed magnetic field, are also plotted on these

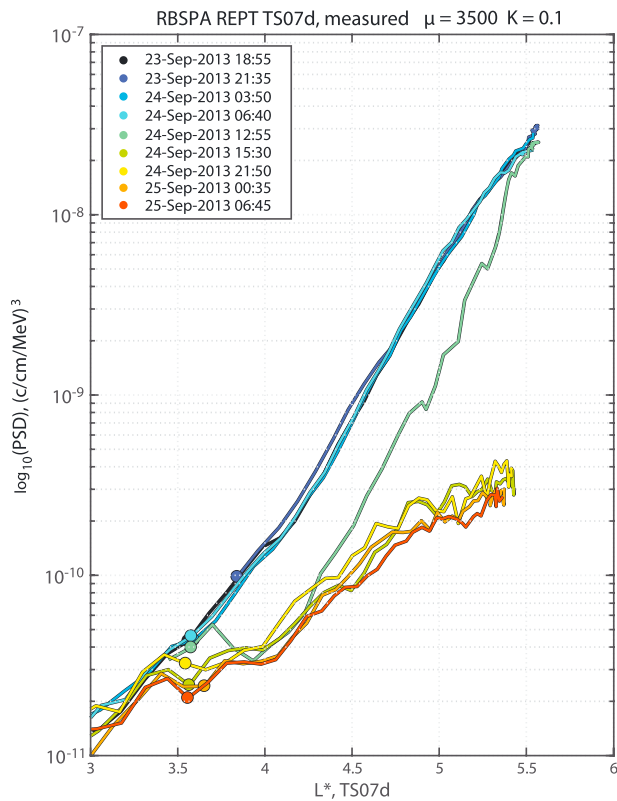


Figure 8. Phase space densities (PSDs), in units of $(c/cm/MeV)^3$, of ultrarelativistic electrons with $\mu = 3,500$ MeV/G and $K = 0.1 G^{0.5} R_E$ observed by Van Allen Probe A during its passes from 18:55 universal time 23 September through 06:45 universal time 25 September 2013. Each filled circle corresponds to the closest point in time when a valid PSD observation was available near a given L^* value of interest, in this case $L^* = 3.6$. These times are given in the legend of the figure, next to the corresponding color. Values of L^* were calculated based on the TS07d magnetic field model. RBSPA = Radiation Belt Storm Probe A; REPT = Relativistic Electron-Proton Telescope.

spectrograms in red, yellow, and white, respectively. Figures 6d and 6e show the ellipticity and wave normal angle of the wave, respectively, and Figure 6f shows the electron density measured by the EFW instrument, indicating a gradual density increase as the spacecraft proceeded inbound from $L = 5.6$ to 3.6 in the afternoon sector. Strong to intense EMIC waves were observed by Van Allen Probe A near 20 MLT from 11:40 UT (1.2-nT rms) at $L = 5$ to 12:50 UT (16.4-nT rms) at $L = 3.9$. Van Allen Probe A also observed strong EMIC waves (2.9-nT rms in the He band and 0.6-nT rms in the H band) from $L = 5$ to 5.5 near 17 MLT from 16:40 to 17:25 UT (shown in Figure 7c) during the following outbound pass. Additional context for this event is provided in Figures 3 and 4 of Su et al. (2016) that show Van Allen Probes A and B observations from multiple instruments from 00:00 to 20:00 UT on this day.

Figure 7 shows simultaneous ground and Van Allen Probe A wave observations between 10:00 and 18:00 UT on 24 September 2013. Figures 7a and 7b are uncalibrated spectrograms from Sodankylä, Finland, and Magadan, Russia, respectively. Figure 7c shows 0- to 1-Hz spectrograms from Van Allen Probe A during its inbound and outbound passes. No wave activity was observed by Probe A during its pass through perigee. Figure 7d is a map showing the Northern Hemisphere magnetic footprint of Van Allen Probe A from 10:00 to 18:00 UT. The magnetic footprint of Probe A was northeast of Uzur, northwest of Magadan, and at somewhat higher $L (= 4)$ when it observed an intense ~ 1.2 -Hz EMIC wave at 12:45 UT. Comparison of Figures 7b and 7c indicates that very similar wave activity appeared at Probe A and Magadan. The Magadan and Uzur spectrograms show that activity continued past 13:00 UT, during the subsequent perigee pass of Probe A. Also shown in Figure 7d is the location of the magnetic footprint of Probe A from 16:00 to 18:00 UT, south of Iceland and ~ 2 -hr MLT west of Finland during its subsequent outbound pass. Comparison of Figures 7c and 7a shows that roughly similar 0.2–0.5-Hz wave activity was observed by Probe A at $L = 5.2$ and at Sodankylä (at the same L shell).

Figure 7d also shows the magnetic footprints of two POES proton precipitation events: a moderate intensity event observed by NOAA 16 north of Irkutsk, Russia, near $L = 3.6$ at 13:13 UT, and a strong precipitation event observed by NOAA 18 over Norway near $L = 5.2$ at 13:50 UT. The NOAA 16 event at 13:13 UT gives evidence that the wave activity observed by Van Allen Probe A from 11:00 to 13:00 UT extended down to slightly lower L shells. The NOAA 18 precipitation event at 13:50 UT was likely to originate in the same wave event observed by the Finnish chain at this time, assuming either that the wave region was extended 15° in longitude or that horizontal ducting brought the wave signal from Norway 15° eastward to Finland.

All the EMIC wave activity recorded by Van Allen Probe A from 10:30 to 17:00 UT was thus also recorded on the ground, and the combination of these data sets provides evidence of intense 0.2–0.5-Hz EMIC wave activity, most likely in the He band, in both east Asia and northern Europe near $L = 5.2$ during much of this time interval.

Figure 8 shows a plot of phase space densities of ultrarelativistic electrons with $\mu = 3,500$ MeV/G and $K = 0.1 G^{0.5} R_E$ observed by Van Allen Probe A during its passes from 18:55 UT 23 September through 06:45 UT 25 September 2013. Values of L^* were calculated based on the TS07d magnetic field model. A broad, deepening minimum was observed between $L^* = 3.4$ and 5.4 beginning on 24 September near 12:00 UT and continuing until 06 UT 25 September, although some recovery occurred near 21:50 UT 24 September. The phase space density profile also showed very little change or increase during the two subsequent days, 25 and 26 September.

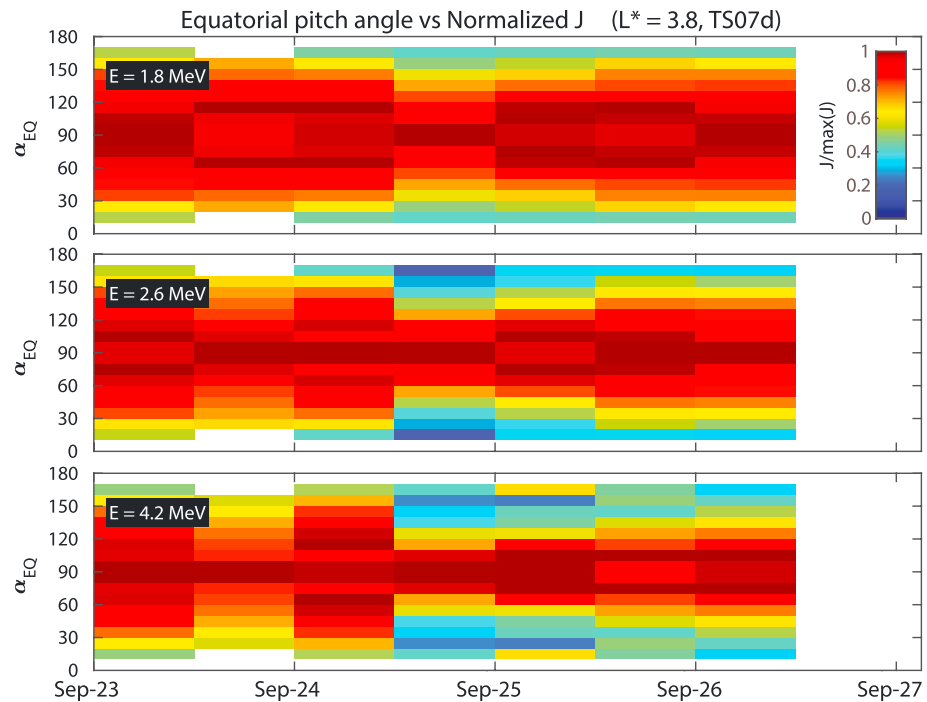


Figure 9. Normalized (to maximum flux over all pitch angles, during a given time interval) equatorial pitch angle distributions of Van Allen Probes Relativistic Electron-Proton Telescope data at $L^* = 3.8$ from 23 to 27 September 2013, for electrons with energies of 1.8, 2.6, and 4.2 MeV. The equatorial pitch angle was computed using the TS07d magnetic field model.

A phase space plot using Van Allen Probe B data with the same parameters as in Figure 8 showed similar variations but was incomplete because of the observational geometry. A plot using $\mu = 2,500$ MeV/G and $K = 0.2$ G^{0.5} R_E provided continuous coverage in L^* and showed a very similar localized minimum, with the lowest values between 12:00 and 21:00 UT on 24 September (supporting information Figure S1). Phase space densities on 24 September for relativistic energies ($\mu = 700$ MeV/G and $K = 0.1$ G^{0.5} R_E) increased monotonically with L^* and gave no evidence of a dip during this time interval (Figure S2). Plots similar to Figure 8 made using other magnetic field models (T89 and T04s) showed a dip that was generally similar in amplitude, radial extent, and timing (not shown).

If EMIC waves are responsible for this localized minimum, then one might expect a narrowing of the pitch angle distribution at ultrarelativistic energies (greater than 2 MeV; Kersten et al., 2014; Usanova et al., 2014). Figure 9 shows the normalized equatorial pitch angle distributions of electron number fluxes at $L^* = 3.8$ for energies of 1.8, 2.6, and 4.2 MeV from 00:00 UT 23 September to 12:00 UT 26 September, with 12-hr resolution, based on data from both Van Allen probes. A substantial narrowing of the distribution toward a peak near 90° that was progressively stronger at higher energies appeared in the 24 September 12:00–24:00 UT interval and gradually broadened in the three subsequent intervals. Figure 9 is based on use of the TS07d model, but very similar narrowing and gradual broadening was observed in figures based on the T89 and TS05 models and using all three models at neighboring L^* values as well.

More accurate timing of the onset of the pitch angle narrowing is provided by plots showing the observed pitch angle distributions as it passed from $L^* = 3.7$ to 3.9 both outbound and inbound during each 9-hr orbit of the Van Allen Probes from 23 through 27 September (not shown): The narrowing first appeared in Van Allen Probe A data during its outbound pass near 15:36 UT, approximately 2 hr after the intense EMIC wave activity recorded by Van Allen Probe A in this L^* range, between 12:44 and 12:51 UT (Figures 6 and 7). These plots also showed a gradual broadening of the pitch angle distributions over the next few days (consistent with Figure 9), such that the distributions at the higher energies remained significantly narrower than those on 23 September through at least 27 September. The location and timing of this narrowing agrees with the

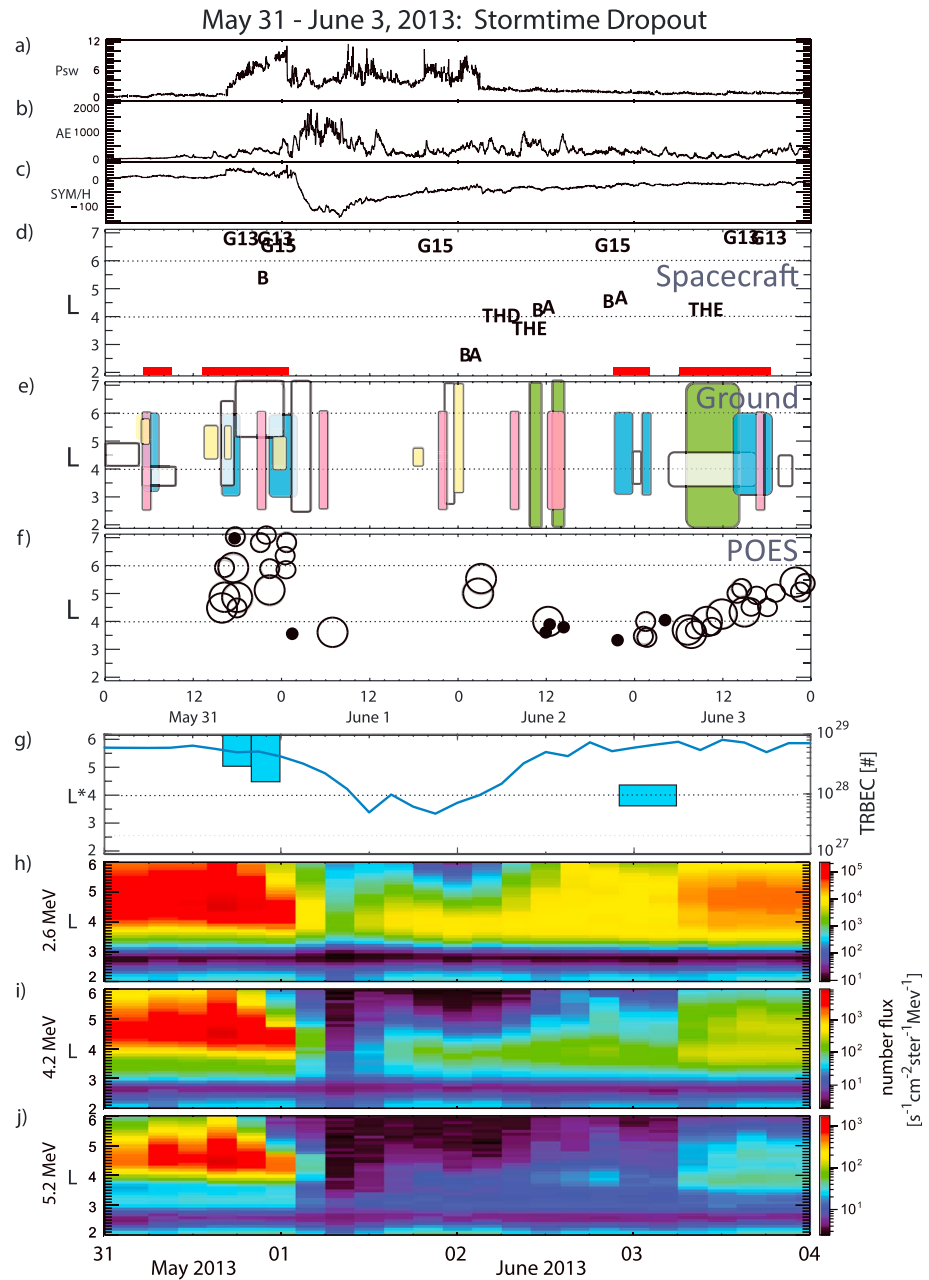


Figure 10. Same as Figure 5, for the stormtime dropout interval from 31 May through 3 June 2013. The red bars in (d) indicate intervals of ground-based observations of intense electromagnetic ion cyclotron waves. POES = Polar Operational Environmental Satellite; TRBEC = total radiation belt electron content.

observed minima in phase space density, and the timing agrees with the Van Allen Probes, ground array, and POES observations as well.

4.2. Stormtime Dropout Interval: 31 May 31 to 3 June 2013

Figures 10a–10c summarize the geomagnetic context of the stormtime dropout event of 31 May to 4 June 2013. Figure 10a shows a modest rise in Psw from 1.5 to 2 nPa at 06:00 UT and a sharp rise in Psw at 14:00 UT on 31 May 2013 that peaked at 11.2 nPa at 00:38 UT and then fell to values near 4 nPa. The rise in Psw preceded by 12 hr the onset at 02:00 UT 1 June 2013 of a magnetic storm (minimum SYM/H = –137 nT) at

07:48 UT (Figure 10c) with an extended recovery phase. The AE index (Figure 10b) peaked at 1,767 nT at 03:57 UT but exhibited significant activity through 3 June.

Figure 10d shows that GOES 13 and 15, Van Allen Probes A and B, and THEMIS D and E all observed wave activity during this 4-day interval. GOES 13 observed intense EMIC waves during two intervals on 31 May: up to 3-nT rms amplitude, 0.2–0.5-Hz He band EMIC waves from 16:20 to 18:20 UT, and ~2-nT rms amplitude, 0.2–0.4-Hz He band waves from 18:20 to 21:10 UT, and GOES 15 observed ~2-nT rms amplitude 0.3–0.55 Hz He band waves between 22:40 31 May and 01:30 UT 1 June, all during the prestorm compression. GOES 15 also recorded ~1-nT rms amplitude bursts of 0.8–1.0-Hz H band EMIC waves from 19:00 to 22:00 UT 1 June, during another interval of increased Psw (Figure 10a), and ~0.5-nT rms amplitude 0.5–0.7-Hz H band waves near 21:00 UT 2 June, and GOES 13 recorded ~1.5-nT rms amplitude 0.5–0.7-Hz H band waves between 14:20 and 17:50 UT 3 June.

Van Allen Probe B observed 2.1 to 3.6-nT rms amplitude 0.2–0.3-Hz He band waves on 31 May from 19:20 to 20:10 UT as it traveled inbound from $L = 5.8$ to 5.6 (MLT 21.9 to 22.5) along a gradual plasma density gradient ($n \sim 30 \text{ cm}^{-3}$). On 2 June, both Probes A and B observed 1.5-nT rms amplitude 2.2-Hz He band waves near 01:50 UT and 2.4 MLT well inside the plasmopause ($n \sim 500 \text{ cm}^{-3}$) at $L = 2.8$. These spacecraft also observed EMIC waves during two intervals later that day. From 13:38 to 13:58 UT during an outbound pass, Probe A observed 0.6-nT rms amplitude 0.85-Hz He band wave activity from $L = 4.3$ to 4.7 near 19.8 MLT, ending at the plasmopause, where the plasma density dropped from 30 to 10 cm^{-3} . At nearly the same time, Probe B observed strong 3.1-nT rms amplitude 0.8-Hz He band waves from 13:30 to 13:46 UT as it passed outbound from $L = 4.3$ to 4.6 near 19.7 MLT, while the plasma density dropped from 100 to 30 cm^{-3} . Probe B also observed weaker (0.3-nT rms) 1.5-Hz H band waves at the same time. From 22:35 to 22:55 UT, again during an outbound pass, Probes A and B observed 0.3-Hz He band waves, with rms amplitudes of 1.2 and 2.2 nT, respectively, from $L = 4.6$ to 5.0 near 19.7 MLT in a region with nearly constant $\sim 150\text{-cm}^{-3}$ plasma density just earthward of a gradual plasmopause.

Three moderate-amplitude EMIC wave events were also observed by THEMIS spacecraft during this interval, all near local midnight: 0.3-nT rms amplitude 0.3–0.4-Hz He band EMIC waves were observed by THEMIS D from 06:49 to 06:57 UT 2 June 2013 as the spacecraft passed outbound from $L = 4.0$ to 4.3 and MLT = 00:16 to 00:27; 0.4-nT rms amplitude He band EMIC waves with frequency falling from 1.3 to 1.0 Hz were observed by THEMIS E from 09:41 to 09:52 UT, also on 2 June, as the spacecraft passed outbound from $L = 3.6$ to 4.1 and MLT from 00:03 to 00:20; and 0.2-nT rms amplitude 1.0-Hz He band EMIC waves were also observed by THEMIS E from 08:45 to 08:48 UT 3 June 2013 as the spacecraft passed outbound near $L = 4.1$ and 00:25 MLT.

Figures 10e and 10f show that numerous EMIC wave events were recorded worldwide during this stormtime interval by ground-based induction coil magnetometers and by the POES spacecraft. We focus here on the four intervals of intense ground activity indicated by the red bars in Figure 10d.

4.2.1. 05:00 to 09:00 UT 31 May

Strong 0.35-Hz EMIC waves were observed at Ivalo ($L = 5.6$) and Sodankylä ($L = 5.2$), Finland, from 05:00 to 05:30 UT, and strong 0.2–0.8-Hz waves were observed at the lower latitude CARISMA stations Pinawa ($L = 4.00$) and Thief River Falls ($L = 3.54$) from 05:00 to 09:00 UT. Intense 0.5–1.2-Hz EMIC waves were observed at Halley from 05:30 to 06:30 UT, but because only one station was available, the location of the waves in L was uncertain. Despite the widespread and strong EMIC wave activity, no depletions appeared in the TRBEC (Figure 10g) or in any of the electron energy channels shown in Figures 10h–10j between 02:00–06:00 UT and 06:00–10:00 UT.

4.2.2. 13:00 UT 31 May to 01:00 UT 1 June

Strong and/or intense EMIC waves were observed by ground-based induction magnetometers at several longitudes between 13:00 31 May and 01:00 UT 1 June. Intense waves were observed at Halley ($L = 4.70$), especially between 16:00 and 18:00 UT. Data from the Finnish chain indicated that waves in the Scandinavian sector between 13:00 and 24:00 UT were above $L = 4$, and data from the CARISMA array indicated that waves in the Canadian sector between 16:00 and 24:00 were localized between $L = 5$ and 7 .

A moderately close ground-satellite conjunction occurred late on 31 May (not shown). As shown in Figure 11, Van Allen Probe B observed strong 0.2–0.3-Hz He band EMIC waves (up to 3.5-nT rms) at $L = 5.8$ – 5.6 in a

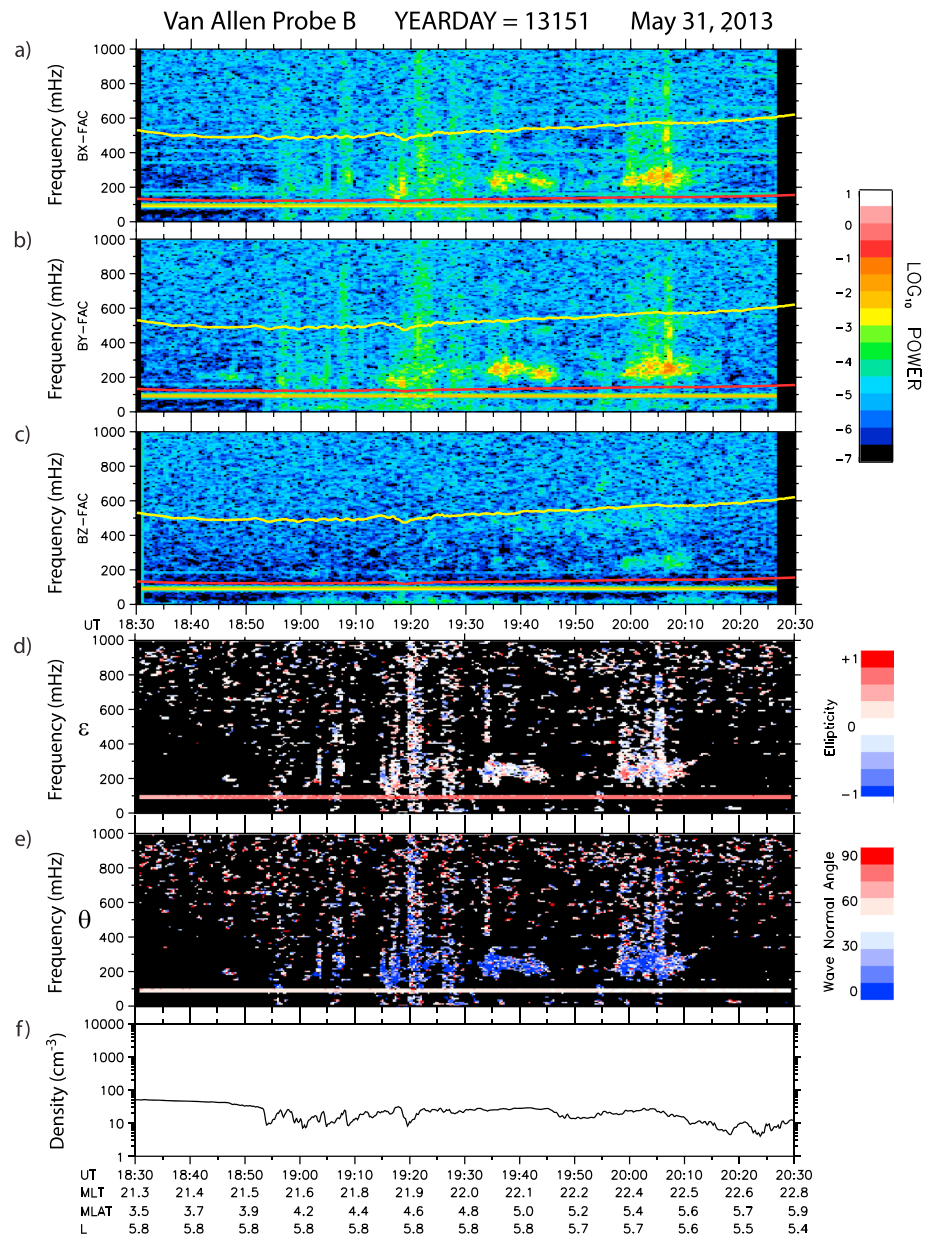


Figure 11. Van Allen Probe B Electric and Magnetic Field Instrument Suite and Integrated Science magnetic field data and Electric Fields and Waves plasma density data from 18:30 to 20:30 UT 31 May 2013 as in Figure 6. UT = universal time; MLT = magnetic local time; MLAT = magnetic latitude.

region with plasma density near $\sim 30 \text{ cm}^{-3}$ as it passed near its apogee over the Kola Peninsula northeast of Finland from 19:20 to 20:10 UT, part of the interval between 19:00 and 23:00 UT when 0.1–0.4-Hz EMIC waves were observed at Ivalo ($L = 5.84$). Probe A passed slightly westward (20-min MLT) of Probe B at nearly the same latitude but saw very little EMIC wave activity. There were no other good conjunctions between Probes A and B and ground-based induction magnetometers on this day.

There was only a slight decrease in TRBEC between 12:00 and 20:30 UT 31 May (Figure 10g).

Significant decreases in 4.2- and 5.2-MeV ultrarelativistic electron flux occurred between 14:00–18:00 and 18:00–22:00 UT (Figures 10i and 10j), but only a slight decrease was evident in the 2.6-MeV electron channel (Figure 10h). Fluxes between $L = 5$ and 6 decreased in all three energy ranges but again were more significant in the higher energy channels (Figures 10i and 10j). Fluxes in all three channels also decreased from

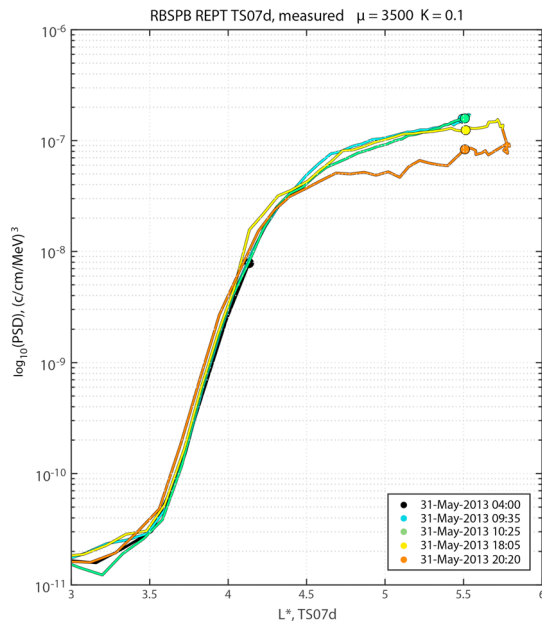


Figure 12. Phase space densities (PSDs) observed by Van Allen Probe B between 04:10 and 22:00 universal time 31 May 2013 as in Figure 8. The filled circles were manually chosen to correspond to the closest point in time when valid PSD observations were available near the $L^* = 5.5$. Rbspb = Radiation Belt Storm Probe B. REPT = Relativistic Electron-Proton Telescope.

18:00–22:00 UT to 22:00–02:00 UT on 1 June at L shells above ~ 4.8 , again with more significant decreases in the higher energy channels.

The phase space density profiles shown in Figure 12 appear to confirm these depletions: the trace at 20:20 UT shows a depletion between $L^* = 4.5$ and 5.8 (the apogee during this pass). The normalized pitch angle plots shown in Figure 13 are also consistent with the EMIC waves being the source of these depletions: energy-dependent narrow peaks at 90° in the 12–24 UT 31 May time bin were evident in the $L^* = 4.8$ and 4.4 panels, but the distribution at $L^* = 3.8$ was much less tightly localized at the higher energies. However, there was no clear deepening minimum in phase space density at a specific L^* value, and narrowing in the pitch angle distribution can be caused by adiabatic effects associated with magnetotail stretching, which is more prevalent at higher L^* . Hence, although the phase space density depletion and pitch angle distribution narrowing may be related to EMIC wave scattering, this cannot be confirmed using the Van Allen Probes data alone.

An order-of-magnitude drop in TRBEC between 20:30 31 May and 12:00 1 June UT (Figure 10g) is also reflected in the drop in electron flux shown in Figures 10h–10j during this same interval. There was very little EMIC activity after 01:00 UT on 1 June, during the main phase of the storm, and that activity was weak. The absence of any EMIC signature, such as narrowing of the flux peak to near 90° in the pitch angle distribution plots in Figure 13 on this day or in phase space density plots (not shown), is consistent with the conclusion of Kang et al. (2018), based on a comparison of Van Allen Probes observations with

the outputs of the CIMI model, that the sudden deep drop in TRBEC and in fluxes in all three energy channels during this interval was caused by magnetopause shadowing and drift loss.

4.2.3. 21:00 UT 2 June to 02:00 UT 3 June

Between 21:00 and 24:00 UT (18–21 MLT) on 2 June, Halley observed intense 0.1–1.0-Hz waves and between 01:00 and 02:00 UT (22–23 MLT) on 3 June strong 0.8–1.2-Hz waves. Two nearby POES passes provided information on the L shells on which these waves occurred. NOAA 15 observed intense proton precipitation at 22:34 UT at $L = 4.1$ on a south polar pass 2 hr west of Halley. Although the flux of this event may thus be unreasonably high because the pass was within the South Atlantic Anomaly (and thus this event is not included in Figure 10f), it still provides corroboration of the Halley EMIC wave observation. A MetOp 1 pass 2 hr west of Halley in MLT observed moderately strong precipitation at $L = 3.7$ at 01:26 UT.

Figure 14 shows 0- to 1-Hz magnetic field spectrograms from Van Allen Probe B (Figure 14a) and Halley, Antarctica (Figure 14b), from 22:00 to 24:00 UT 2 June 2013. During this interval, both Van Allen Probes A and B passed very near Halley, Antarctica, as they approached their apogee (Figure 14c). Both probes observed only modest EMIC activity for ~ 10 min near 22:40 UT, but Halley observed multiple wave bands for over an hour, from 22:23 to 23:35 UT: the same wave band (0.35 Hz) as observed at Probes A and B, an intense higher frequency band (0.4–0.6 Hz), and a somewhat weaker band at even higher frequencies (0.8–1.3 Hz). Comparison of these spectrograms suggests, in light of the NOAA 15 observations of intense proton precipitation, that the 0.4–0.6-Hz EMIC waves observed at Halley originated on L shells somewhat lower than those traversed by the Van Allen Probes.

Figure 10g shows very little change in TRBEC between 18:00 2 June and 06:00 3 June UT, consistent with little or no decrease in the electron flux in the 2.6-MeV channel (Figure 10h), but decreases were observed over a broad L range during this interval in the 4.2- and 5.2-MeV energy channels (Figures 10i and 10j). Figure S3 shows phase space density profiles from 04:25 UT 2 June through 21:55 UT 3 June for $K = 0.1 G^{0.5} R_E$. Unfortunately, the profile at the time of these flux decreases (04:35 UT), extended only inward from $L^* = 3.6$ because of the far off-equatorial location of both Van Allen Probes (nearly 19°), which were in nearly coincident orbits at the time. Figure S3 does show a flattening of the profiles during the 22:25 UT pass between $L^* = 3.6$ and 4.2 and a steepening between $L^* = 4.2$ and 4.4, with the lowest

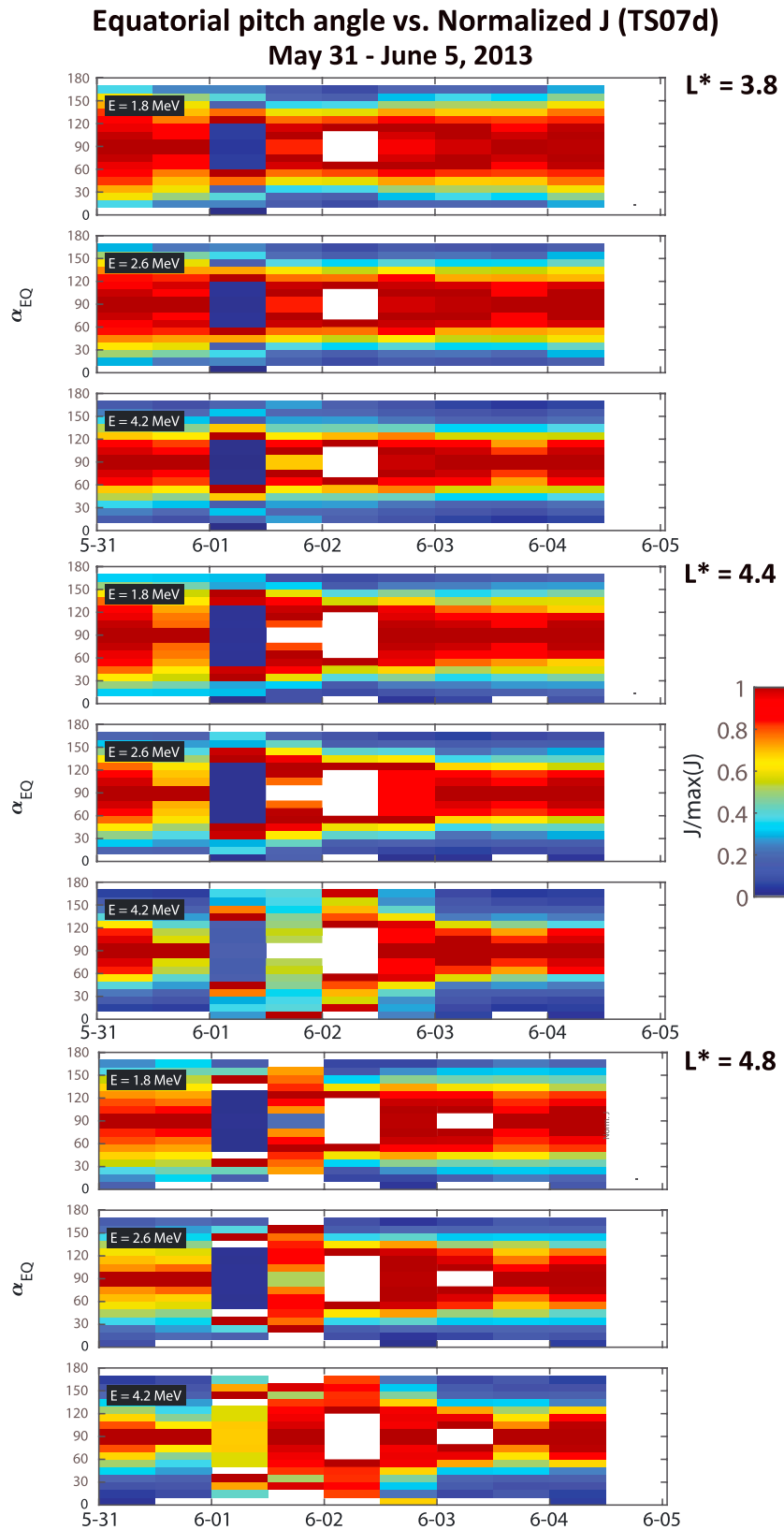


Figure 13. Normalized pitch angle distributions of Van Allen Probes Relativistic Electron-Proton Telescope data at $L^* = 3.8$, 4.4, and 4.8 from 31 May to 5 June 2013 for electrons with energies of 1.8, 2.6, and 4.2 MeV, using the TS07d magnetic field model.

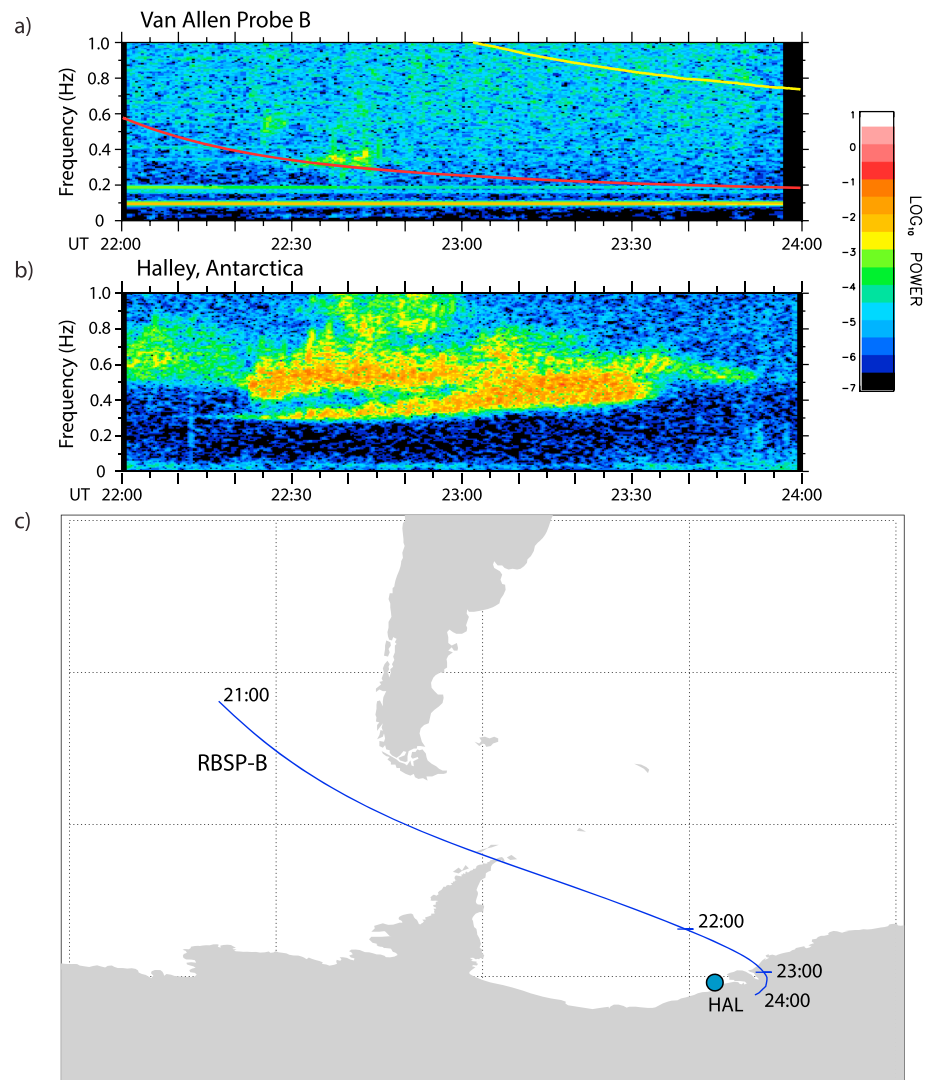


Figure 14. Composite figure showing spectrograms of the radially outward transverse component of Electric and Magnetic Field Instrument Suite and Integrated Science magnetic field data from Van Allen Probe B (a) and the north-south component of induction coil magnetometer data from Halley, Antarctica, from 22:00 to 24:00 UT 2 June 2013 (b) and a map showing the Southern Hemisphere magnetic footprint of Van Allen Probe B from 21:00 to 24:00 UT 2 June 2013 (c). The position of Halley is indicated by the blue circle. UT = universal time.

values in the L^* range between 3.6 and 4.5. This is roughly consistent with the timing and L range of the EMIC activity in the Halley and POES data. Figure 15 shows phase space density profiles for $K = 0.2 G^{0.5} R_E$, which do include data for a full pass during the time of the missing data in Figure S3. This figure and a very similar one for Probe B (not shown) both showed a clear minimum in phase space density between $L^* = 3.6$ and 4.1 during the 04:20 UT pass that was fully filled in by the time of the 07:40 UT pass. The times of both this minimum and the subsequent recovery match the time of the minimum flux values and subsequent increase in Figures 10i and 10j. The pitch angle distributions shown in Figure 13 from 0 to 12 UT on 3 June at $L^* = 3.8$ and 4.4 were narrower than those for the previous 12 hr, but the narrowing was only slightly greater for higher energies.

4.2.4. 06:00 UT to 18:00 UT 3 June

Intense 0.7–1.5-Hz EMIC waves were observed between 03:00 and 15:00 UT (21:00–09:00 MLT) at the two lowest latitude CARISMA stations, Thief River Falls ($L = 3.54$) and Pinawa ($L = 4.00$), and intense waves with similar but gradually rising frequencies were observed at Halley from 13:00 to 18:00 UT (10:00–15:00 MLT). Waves were also observed at East Asian and Russian stations. Numerous intense POES precipitation events

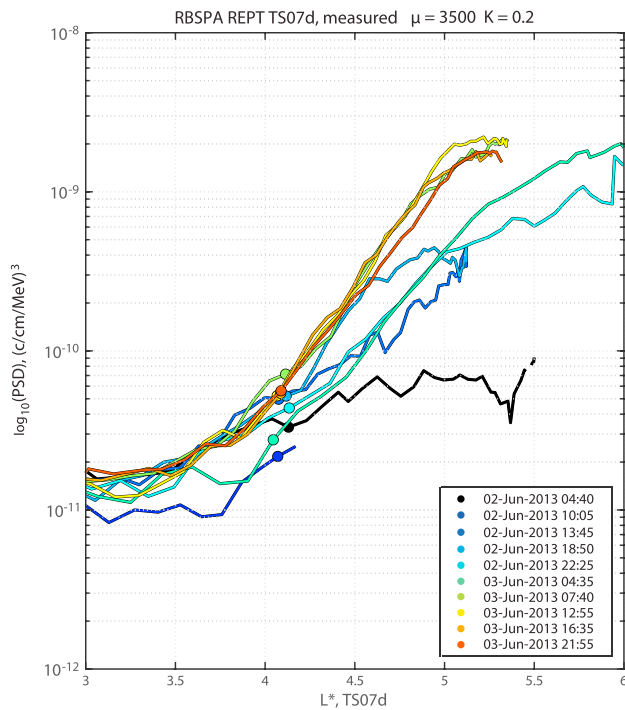


Figure 15. Phase space densities (PSDs) observed by Van Allen Probe A between 04:40 universal time 2 June 2013 and 21:55 universal time 3 June 2013 as in Figure 8 but for $K = 0.2 \text{ } 1 \text{ } G^{0.5} \text{ } R_E$. The filled circles were manually chosen to correspond to the closest point in time when valid PSD observations were available near $L^* = 4.1$. RBSPA = Radiation Belt Storm Probe A; REPT = Relativistic Electron-Proton Telescope.

were recorded during this same interval, beginning near $L = 3.5$ at 06:00 UT and rising gradually to $L = 5.5$ near 23:00 UT.

Although little increase in TRBEC was observed during this interval (Figure 10g), REPT data in Figures 10h–10j shows that fluxes in all three channels increased above $L = 3.5$ from 02:00–06:00 UT to 06:00–10:00 UT and continued to increase through 14:00–18:00 UT, indicating the presence of flux enhancement processes that might counteract any EMIC-related losses, but these panels also reveal a narrow L range centered near 4.2 with lower flux levels in the 4.2- and 5.2-MeV channels that persisted until the end of the day. The phase space densities in Figure 15 during 3 June continued to show a flattening of the profiles between $L^* = 3.6$ and 4.2 and a steepening between $L^* = 4.2$ and 4.4, and the pitch angle distributions in Figure 13 show that the narrowing at 4.2 MeV increased at $L^* = 3.8, 4.4,$ and 4.8 from the first half of 3 June through the second half and showed only a modest broadening at 4.2 MeV during the first half of June 4.

4.3. Stormtime Enhancement: 17–19 March 2013

Baker et al. (2014) provided the context for this event, presenting changes in both multi-MeV electron flux and phase space density changes during March 2013 as well as 2.8-MeV electron flux from 12:00 UT 16 March through 00:00 UT 19 March, and Foster et al. (2014) provided details of the acceleration process, in particular that the acceleration occurred outside the plasmopause. Several papers have also presented simulations of the depletion and enhancement that occurred during this interval. Ukhorskiy et al. (2015) simulated the depletion that occurred at the beginning of this event near 06:00 UT on 17 March and concluded that losses for $L > 5$ were related to transport across the magnetospheric boundary, and losses for $L < 5$

were related to adiabatic processes. Z. Li, Hudson, et al. (2014) showed that although radial diffusion alone was consistent with observations for three of four enhancements in phase space density during the month of March 2013, an additional, local acceleration mechanism would be needed in order to match observations during the 17 and 18 March enhancement. W. Li, Thorne et al. (2014) simulated the effects of whistler-mode chorus observed by the Van Allen Probes during this enhancement and found very good agreement between simulated and observed electron phase space density near the location of its radial peak. Xiao et al. (2014) calculated drift and bounce-averaged diffusion coefficients based on observed chorus spectra and used them in numerical simulations to demonstrate that the observed lower-band chorus waves could cause the observed increase in electron fluxes within 15 hr. Wang et al. (2017) concluded that the rapid enhancement of radiation belt flux resulted from the combination of transport by radial diffusion of a seed electron population and subsequent local acceleration driven by chorus waves, and Ma et al. (2018), who incorporated both local electron heating by chorus waves and radial transport in their simulation, concluded that resonant interaction with chorus waves was the dominant process that accounted for the electron flux enhancement, particularly near the location of the flux peak.

Figure 16a shows a sudden jump in solar wind pressure associated with an interplanetary shock near 06:00 UT on 17 March from ~ 1 nPa to over 7 nPa. This increase, along with a sharp southward deflection of the interplanetary field (B_z fell rapidly from -4 nT at 05:40 UT to -10 nT at 06:00 UT), was reflected almost immediately in an increase in the AE index from below 100 nT to over 1,000 nT (Figure 16b), and a jump in SYM/H from 10 to +35 nT (Figure 16c). The AE index remained steady near 50 nT from the beginning of 18 March until it rose again at 19:00 UT 19 March, but Psw increased by 50% or more above 1.5 nPa during several intervals during these days.

THEMIS E observed a 5-nT rms amplitude 0.5-Hz He band EMIC wave at 07:46 UT 17 March as it passed $L = 6.6$ outbound near 06:12 MLT (Figure 16d). GOES 13 observed moderate intensity 0.6–0.95-Hz H band EMIC waves from 16:50 to 18:20 UT (11:50–13:20 MLT) 18 March, strong 0.4-Hz He band waves from 18:10 to

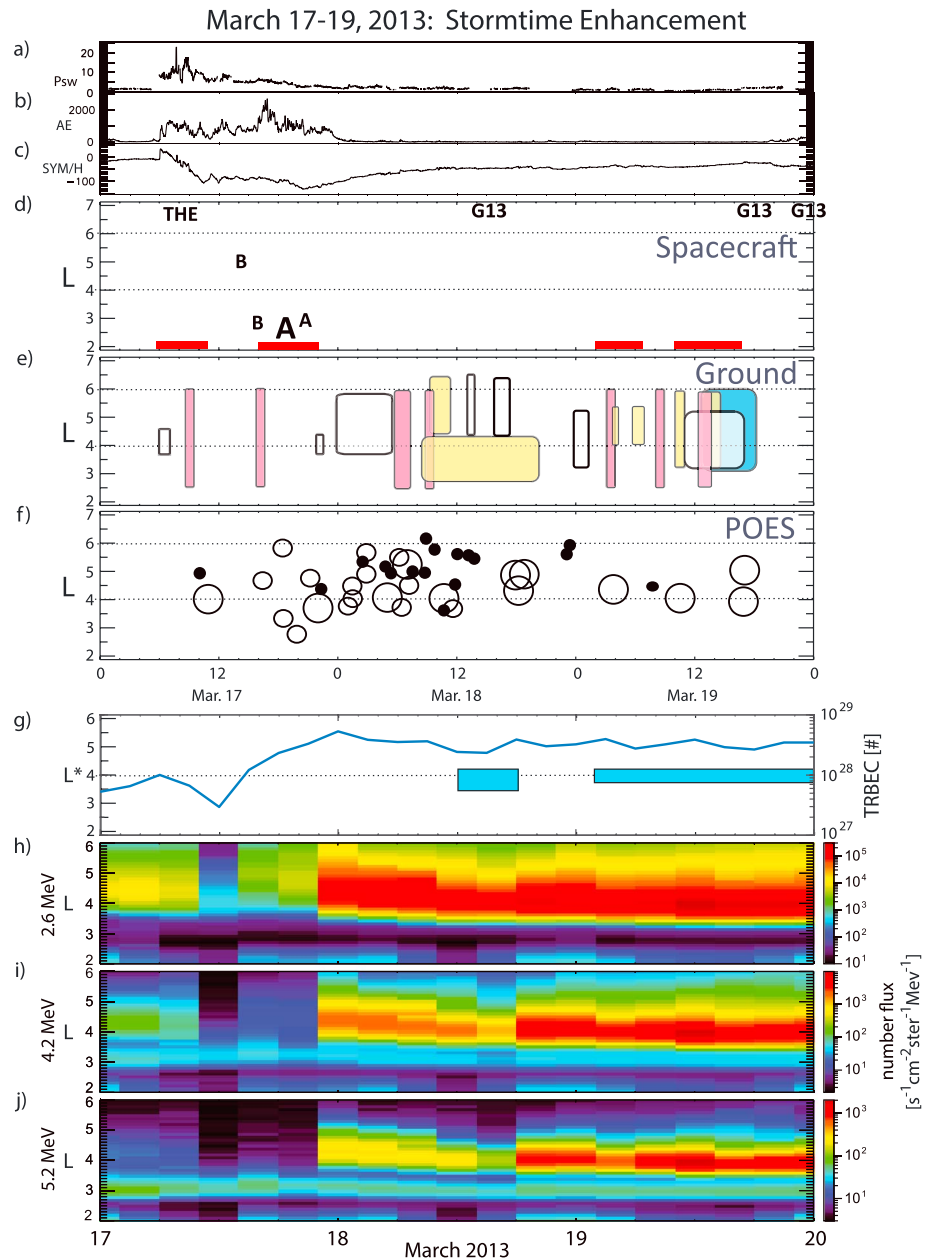


Figure 16. Same as Figure 5, for the stormtime enhancement interval from 17 through 19 March 2013. The red bars in (d) indicate intervals of ground-based observations of intense electromagnetic ion cyclotron waves. POES = Polar Operational Environmental Satellite; TRBEC = total radiation belt electron content.

18:40 UT (13:11–13:41 MLT) 19 March, and strong 0.4–0.5-Hz H band waves from 23:20 to 23:30 UT (18:10–18:20 MLT) 19 March, each during intervals of greatly or slightly increased Psw. However, only during the second half of 17 March were any waves observed by equatorially orbiting spacecraft below $L = 6$. One intense wave event (6.2-nT rms amplitude, 3.5 Hz) was observed by Van Allen Probe A near $L = 2.5$ and 5.1 MLT at 18:25 UT, and two moderate-amplitude waves were observed near $L = 2.9$: 1.0 nT rms amplitude, 2.2–3.7 Hz by Probe B from 17:00 to 17:15 UT near 4.5 MLT, and 0.6 nT rms amplitude, 1.5 Hz by Probe A at 20:10 UT near 21.2 MLT. Probe B also observed 0.7 nT rms amplitude 0.5 Hz waves near $L = 4.4$ and 2.5 MLT at 16:05 UT.

Many EMIC wave events were recorded during this interval by ground-based induction magnetometers and POES proton detectors (Figures 16e and 16f), and in many instances, mostly on the dayside, there was a good

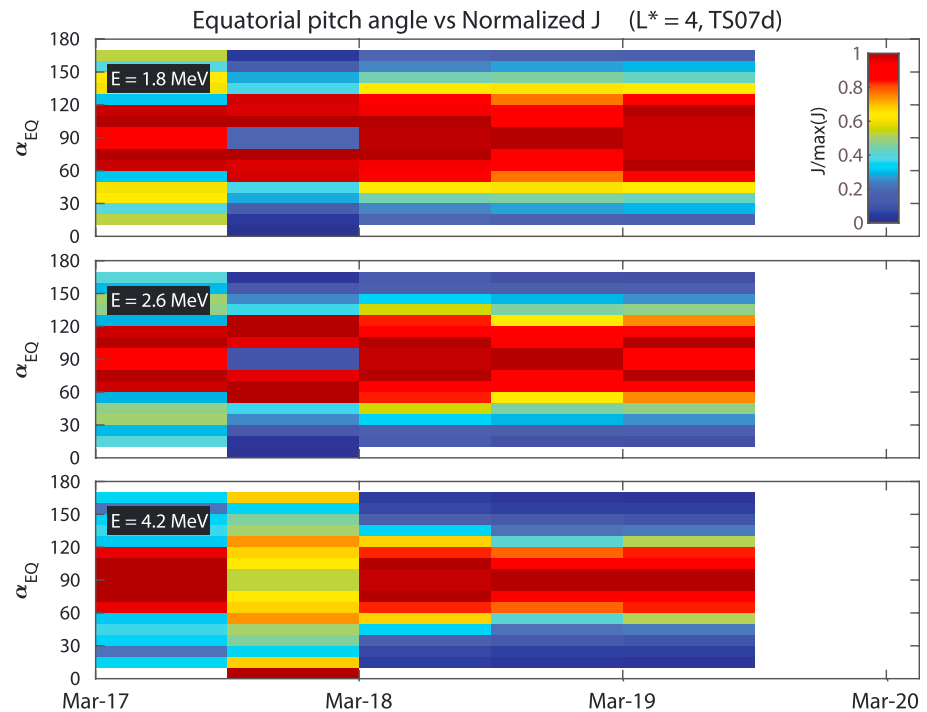


Figure 17. Normalized pitch angle distributions of Van Allen Probes Relativistic Electron-Proton Telescope data at $L^* = 4$ from 17 to 20 March 2013 for electrons with energies of 1.8, 2.6, and 4.2 MeV, using the TS07d magnetic field model.

correspondence in universal time and in L shell between the induction magnetometer and POES observations. Details of these observations can be found in the hourly L versus MLT tables and will not be repeated here.

Figures 16g–16j show two enhancements in relativistic electron fluxes during this 3-day interval, an order of magnitude enhancement in TRBEC during the second half of 17 March and a smaller enhancement near 18:00 UT 18 March (much less evident in the TRBEC trace, which indicates that more of the increase was at higher energies). Four intervals of intense ground activity are indicated by the red bars in Figure 16d, two each on 17 and 19 March. All four of these were associated with modest flux drops in the more energetic channels shown in Figures 16i and 16j, but there was little evidence for the action of EMIC waves in narrowing the pitch angle distributions of ultrarelativistic electrons (Figure 17) during the first two events.

Gradual depletions of flux were evident from 00:00 to 18:00 UT on 18 March in all the energy ranges shown in Figures 16h–16j, consistent with a similar gradual drop in TRBEC. Although there was also considerable EMIC activity on this day, none of the EMIC waves observed on the ground had large amplitude. Only at Nurmijarvi, Finland ($L = 3.44$), was there intermittent wave activity with modest amplitude on 18 March, between 08:00 and 20:00 UT. Because none of the higher latitude stations in the Finnish chain (at $L = 4.56$ and above) observed this activity, its location is marked in Figure 16e with a broad yellow band centered at $L = 3.44$. A more precise location of this event in L is provided by NOAA 19, which was traveling northward at 12.8 MLT (0.4-hr MLT east of Nurmijarvi, over western Russia) and observed a very intense precipitation burst (1.2×10^5 counts $(\text{cm}^2 \text{ s sr})^{-1}$ in the 30–80-keV channel) between 10:22 and 10:23 UT between $L = 3.91$ and 4.06. The effect of this EMIC wave activity may be evident in drops in flux between $L = 3.5$ and $L = 4.5$ in the 4.2- and 5.2-MeV channels (Figures 16i and 16j) from 10:00–14:00 UT to 14:00–18:00 UT that were not accompanied by any drop in the 2.6-MeV channel.

Near the beginning of 19 March, more intense EMIC wave activity occurred and resulted in a drop in ultrarelativistic electron flux from 22:00 18 March–02:00 19 March to 02:00–06:00 19 March that was most prominent between $L = 4.0$ and 4.5 at in the 5.2-MeV channel but also evident between $L = 4.5$ and 5.5 in the lower energy ranges. After two 4-hr intervals showing flux increases in all three energy channels, another

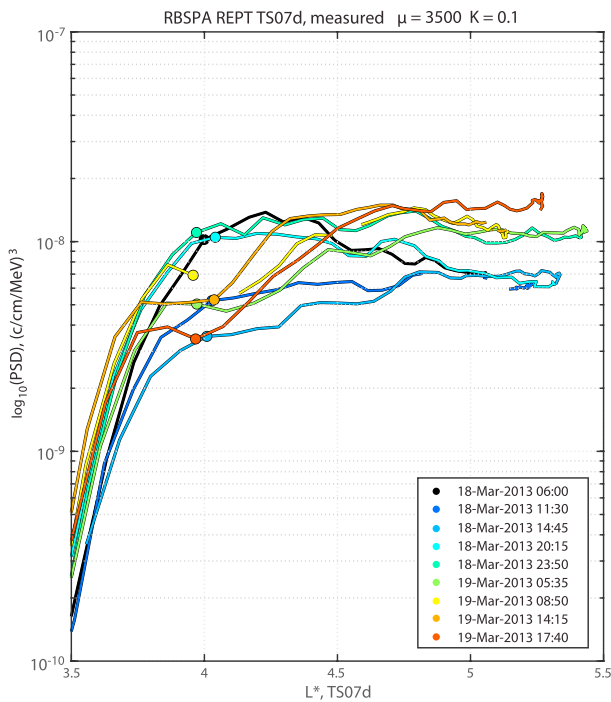


Figure 18. Phase space densities (PSDs) observed by Van Allen Probe A between 06:00 universal time 18 March and 17:40 universal time 19 March 2013 as in Figure 8. The filled circles were manually chosen to correspond to the closest point in time when valid PSD observations were available near $L^* = 4.0$. RBSPA = Radiation Belt Storm Probe A; REPT = Relativistic Electron-Proton Telescope.

energy-dependent flux dropout occurred between 10:00–14:00 UT 19 March and 14:00–18:00 UT 19 March in approximately the same L range.

Figure 17 shows a plot of the normalized equatorial pitch angle distribution at 12-hr resolution of electron number fluxes at $L^* = 4$ in the same format as Figure 9, based on the TS07d magnetic field model. During the first half of 17 March, plots using all three magnetic field models showed broad maxima between 60° and 120° in all three energy ranges. The complex distributions in all three channels during the second half of 17 March, corresponding to the deep flux dropouts shown in Figures 16h–16j, may be statistical artifacts associated with low count rates. During the first half of 18 March, the pitch angle distributions in all three energy ranges were somewhat peaked near 90° but more narrowly peaked at 4.2 MeV, and they became significantly narrower in all three energy ranges during the second half of that day. The narrow peak near 90° in the 4.2-MeV energy range continued with only a slight broadening during the first half of 19 March, even while the peak became significantly broader in the two lower energy ranges. These energy-dependent differences in pitch angle distributions patterns are evidence of the influence of EMIC waves during 19 March (and possibly during the latter half of 18 March) but also indicate the probable influence of other wave-related processes. Figure 18 shows a plot of phase space densities of ultrarelativistic electrons with $\mu = 3,500$ MeV/G and $K = 0.1$ $G^{0.5} R_E$ observed by Van Allen Probe A during its passes from 06:00 UT 18 March through 17:40 UT 19 March 2013. Both this plot and a similar plot of Van Allen Probe B data (Figure S3) show a sequence of a

depletion, recovery, and second depletion. The sequence of black, dark blue, and medium blue traces from 06:00 to 14:45 UT shows a broad drop between $L = 3.8$ and 4.8. The light blue and dark green traces at 20:15 and 23:50 UT on 18 March show that the phase space density levels returned to their earlier higher levels, and the light green, yellow, orange, and red traces show a second and more localized depletion between $L = 3.7$ and 4.3 from 05:35 to 17:40 UT on 19 March. There are gaps in the 08:50 UT (yellow) trace, but there is still a clear dip in the phase space density during this pass. Figure 18 also shows evidence of a deepening of this minimum near 17:00 UT, which correlated with the stronger of the two POES precipitation events shown in Figure 2. A similar plot for relativistic energies (Figure S4) showed that there was no minimum near $L = 4$ at these energies at least until 17 UT 19 March.

4.4. Nonstorm Enhancement: 19–21 September 2013

Ma et al. (2018) simulated the radiation belt fluxes during this event and found, by comparing the effects of local electron heating by chorus waves and radial transport, that radial diffusion by ultralow frequency waves played a dominant role in driving this enhancement at least within the Van Allen Probes orbits ($L < \sim 6$).

Figures 19a–19c provide the geomagnetic context for this event. The solar wind dynamic pressure was below 2 nPa during all parts of this interval except between 08:00 and 10:00 on 19 September (Figure 19a). AE also exhibited a short rise to 1,600 nT during this interval but remained below 500 nT for most of the interval and was often below 100 nT (Figure 19b). The SYM-H index remained between -30 and 0 nT during the entire 3-day interval.

There was considerably less EMIC wave activity during this event than during the others. Only three EMIC wave events were recorded by spacecraft during this event (Figure 19d). GOES 13 observed a 0.7-nT rms amplitude, 0.1–0.3-Hz He band wave at $L = 6.8$ between 22:40 and 23:20 UT on 19 September. Van Allen Probe A observed 6.4-nT rms amplitude, 0.3–0.4-Hz He band waves simultaneous with similar amplitude 0.5–0.6-Hz H band waves between 03:44 and 03:50 UT at its apogee ($L = 5.8$) at 18.1 MLT. Probe B observed strong 5.6-nT rms amplitude 0.2–0.3-Hz He band waves but only weak H band waves, between 08:40 and 08:55 UT near its apogee ($L = 5.9$) at 17.9 MLT. Ground-based

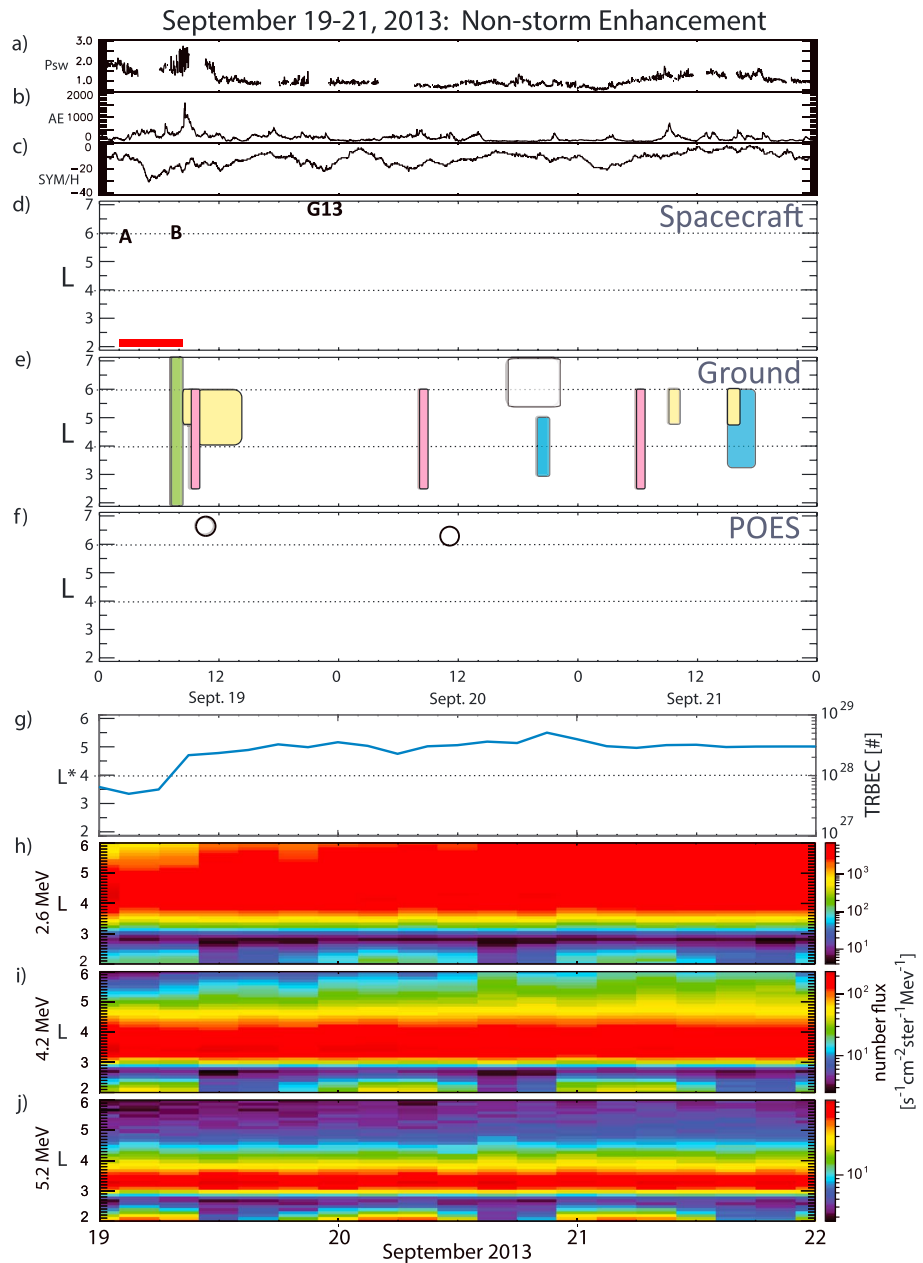


Figure 19. Same as Figure 5, for the nonstormtime enhancement interval from 19 September through 21 September 2013. The red bar in (d) indicates an interval of observations of intense electromagnetic ion cyclotron waves by the Van Allen Probes. POES = Polar Operational Environmental Satellite; TRBEC = total radiation belt electron content.

induction magnetometers at several locations recorded EMIC waves during this 3-day interval (Figure 19e), but none were intense, and Figure 19f shows that only two high-L POES proton precipitation events were observed.

Figure 19g reveals a factor of 3 increase in TRBEC during the first 8 hr of 19 September, which is reflected in a strong increase in the 2.6-MeV electron flux at $L > 5$ (Figure 19h) and steady fluxes during the remainder of the interval. The intense EMIC waves observed by both Van Allen Probes near $L = 6$ between 00:00 and 06:00 UT on this day might be expected to cause significant depletions of the most energetic radiation belt fluxes, but instead, the fluxes even in the 4.2-MeV energy range increased between 02:00–06:00 UT and 10:00–14:00 UT. Consistent with this increase, plots of phase space densities of both ultrarelativistic

Table 3

Upper Bound of the Normalized Frequency of Electromagnetic Ion Cyclotron Waves Observed by Van Allen Probes A and B During the Four Geospace Environment Modeling Quantitative Assessment of Radiation Belt Modeling Challenge Events, Magnetic Latitude of Observation, and Values Extrapolated Along the Magnetic Field Line to the Position of Minimum |B| Using Three Different Magnetic Field Models (Tsyganenko, 1989; Tsyganenko & Sitnov, 2005, 2007)

Date	UT	S/C	Brms (nT)	f_u/f_{He}	MLAT	Equatorial f_u/f_{He}
17 March	16:00	B	0.7	0.56	−0.8	0.566–0.568
17 March	17:05	B	1.0	0.47	4.8	0.476–0.478
17 March	18:25	A	6.2	0.51	3.4	0.516
17 March	20:10	A	0.6	0.43	−7.6	0.508–0.521
31 May	19:35	B	2.1	0.48	4.9	0.618–0.802
31 May	20:05	B	3.6	0.47	5.5	0.590–0.957
2 June	01:43	B	1.5	0.45	9.2	0.495–0.501
2 June	01:56	A	1.5	0.54	9.8	0.588–0.594
2 June	13:40	B	3.1	0.84	−3.6	0.845–0.852
2 June	13:45	A	0.6	0.81	−3.4	0.820–0.826
2 June	22:40	B	1.1	0.29	14.2	0.424–0.486
2 June	22:48	A	2.2	0.41	14.7	0.612–0.701
19 September	03:50	A	6.4	0.92	4.7	0.964–0.982
19 September	08:50	B	5.6	0.69	−5.8	0.761–0.788
24 September	11:45	A	1.2	0.62	−12.4	0.971–1.218
24 September	12:48	A	16.4	0.47	−15.6	0.721–0.793
24 September	13:22	B	2.2	0.93	1.3	0.937–0.939
24 September	16:56	A	2.9	0.80	7.8	0.874–0.906

Note. MLAT = magnetic latitude; UT = universal time.

electrons (3,500 MeV/G; Figure S5) and relativistic electrons (700 MeV/G; Figure S6) showed similar depletions at 06:45 UT above $L = 4.8$, but at all later times during these 3 days, the phase space densities in both μ ranges increased with L^* from 3 to 5.5. This suggests that any EMIC wave-related depletion effects were overcome by enhancement processes.

5. Normalized Frequencies

Gyroresonant interactions of relativistic electrons with EMIC waves are expected to have a much lower energy threshold when the wave frequency is near an ion gyrofrequency (e.g., Figure 3 of Summers & Thorne, 2003). Table 3 shows the upper bound (10% of peak) of the normalized frequency (f_u/f_{He}) of the waves observed by the Van Allen Probes during each of the challenge events, traced along the magnetic field line to the position of minimum |B| using three different magnetic field models: T89 (Tsyganenko, 1989), TS05 (Tsyganenko & Sitnov, 2005), and TS07D (Tsyganenko & Sitnov, 2007).

All four of the wave events observed on 17 March 2013 had upper bounds near $\sim 0.5 f_{He}$, suggesting they would have resonance only above ~ 4 MeV. As noted above, flux depletions were observed during these events, but at L shells that corresponded to dayside POES events rather than these nightside Van Allen Probe events.

The EMIC waves observed by the Van Allen Probes on 31 May 2013 had upper frequency ratios at or above 0.8 and were associated with a decrease in relativistic electron fluxes. Waves observed near $L = 2.5$ and 02:00 UT on 2 June 2013 had low equatorial frequency ratios and weak amplitudes; relativistic electron fluxes in this L shell region were very low, so the effectiveness of these waves is not evident in Figure 10. Waves observed near 14:00 UT on 2 June were also weak but had an upper frequency ratio above 0.8. Relativistic electron fluxes were unaffected or even increased during this interval. Waves observed near 23:00 UT again had low ratios and only moderate amplitudes. As noted above, however, the Van Allen Probes missed the strong EMIC wave activity at this time which occurred at higher frequencies and presumably at lower L values.

The EMIC waves observed by the Van Allen Probes during 19 September 2013 above $L = 5.8$ had large amplitude and large frequency ratios, but again, the fluxes of the higher energy electrons were weak, so they appeared to have no effect.

During the 23–26 September 2013 storm interval, the equatorial f_u/f_{He} ratio was high in all cases. The ratio for the 24 September, 12:48 UT wave event was somewhat lower, but as Su et al. (2016) showed in their Figure 8, the amplitude of this wave was so large that even at the 1% level significant power was present up to 98% of the helium gyrofrequency.

6. Discussion

Narrowing of pitch angle distributions toward 90° has been confirmed as a consequence of EMIC wave activity both in recent modeling results (Kersten et al., 2014; Ni et al., 2015; Su et al., 2016; Usanova et al., 2014) and in observations (Engebretson et al., 2015; Shprits et al., 2016; Usanova et al., 2014; Xiang et al., 2017; X.-J. Zhang, Tu et al., 2016), but as X.-J. Zhang, Li et al. (2016) pointed out, narrowing of observed pitch angle distributions can occur even without the presence of EMIC waves in cases of drift shell splitting. We note also that because EMIC waves cannot by themselves cause scattering of electrons with pitch angles near 90° , they cannot cause precipitation of the bulk of these populations, so phase space densities would be expected to be only modestly reduced by EMIC waves, regardless of their intensity. However, the combined action of EMIC and whistler mode chorus waves to produce rapid dropouts of electrons with energies above ~ 2 MeV has been demonstrated in simulation studies by Mourenas et al. (2016) and confirmed in observations using simultaneous Van Allen Probes and THEMIS data by X.-J. Zhang, Mourenas et al. (2017). This combination of wave effects was also invoked by Boynton et al. (2017) as the cause of the rapid precipitation losses of 1–10-MeV electrons observed by Global Positioning System satellites. The depletion events identified here in association with EMIC waves all show localized phase space depletions as well as at least modest narrowing of the pitch angle distributions, again consistent with the combined action of EMIC and whistler mode waves, but it is beyond the scope of this paper to confirm the existence of that combination in each of these events.

The events studied here have indicated that EMIC waves appear to have major, minor, or in some cases, little or no, effects on the fluxes, phase space densities, and/or pitch angle distributions of radiation belt electrons. Two instances of extended dropouts were clearly associated with EMIC waves both temporally and spatially. The first, during the nonstorm dropout interval described in section 4.1, began near 12:00 UT on 24 September 24 and continued at least through the end of 26 September. The second, which occurred during the end of the stormtime enhancement interval described in section 4.3, began near the beginning of 19 March and continued later that day. In both cases, phase space density plots of ultrarelativistic electrons showed localized depletions and narrowed pitch angle distributions peaked at 90° near $L^* \sim 4$, while lower energy relativistic electrons showed no depletions or narrowing.

EMIC wave activity was associated with more localized and short-lived depletions between 14 and 24 UT on 31 May (centered near $L^* = 5.2$ and 4.8), between 22 UT 2 June and at least 06 UT 3 June (between $L^* = 3.6$ and 4.1), and between 12 and 18 UT on 18 March (between $L^* = 3.5$ and at least 4.2), but EMIC waves observed between 06 and 10 UT and between 16 and 20 UT 17 March, between 05 and 09 UT 31 May, between 08 and 18 UT 3 June, and between 03 and 08 UT 19 September, evidently had lesser or no effects on ultrarelativistic electrons.

For some events, EMIC waves may be observed at times when local minimums are not seen in the data, or vice versa, as a result of competing mechanisms (Aseev et al., 2017). It is beyond the scope of this study to examine the other mechanisms that might counteract the effect of EMIC waves during these latter cases, but we hope that the information provided here will be useful to both modelers and those who can examine and characterize these other mechanisms. Generally, looking at higher L^* data using the *dips&PAD* methodology can be questionable, and it is best applied at lower L^* where one can more easily rule out these other effects (e.g., Shprits et al., 2016).

It is difficult to identify a clear EMIC wave amplitude threshold that distinguishes intervals of phase space density depletions. Most of the intervals of EMIC-induced depletion were identified using ground-based data; ducting effects and frequent lack of calibrations made it impossible to infer in situ amplitudes from these observations. Although some of the intervals of most intense EMIC wave activity were clearly associated with localized depletions of ultrarelativistic electrons, other intervals of intense waves were not. On the other hand, the interval on 18 March that was associated with a phase space density depletion was associated with only moderate amplitude EMIC waves. The situation is complicated because of the presence of multiple

mechanisms that can accelerate or deplete the radiation belts, as well as the limited spatial coverage of both spacecraft and induction coil magnetometers during these challenge events. Based on the events presented here, a reasonable estimate of an EMIC wave amplitude threshold, most applicable below $L^* \sim 5$, is that in situ rms amplitudes >2 nT may be expected to cause detectable depletions.

The impact of EMIC wave activity at or below $L = 3$ has rarely been examined, in part because many fluxgate magnetometers on magnetospheric spacecraft switch to a lower sensitivity range in regions of larger $|B|$ (e.g., Anderson et al., 1992; Meredith et al., 2003). Fortunately, the EMFISIS fluxgate instruments on the Van Allen Probes do not change ranges until $L \sim 2$. This study has identified five EMIC wave events in Van Allen Probes data in this L range, early on 2 June and during the last half of 17 March, all with moderate to large amplitude. Discussion of these events, including their apparent lack of influence on ultrarelativistic electrons on 17 March, will be deferred for future work.

Several of the intervals of intense EMIC wave activity identified in this study that were effective in depleting ultrarelativistic electrons occurred during intervals of high or increasing Psw or injections of plasma from the magnetotail (indicated by increases in the AE index). Increases in both Psw and AE were associated with the EMIC waves on 24 September and on 17 March. The EMIC wave events observed on 31 May and 19 March were associated with only modest increases in Psw and little or no increase in AE, and the wave events observed on 3 June were associated with modest increases in AE. This pattern is consistent with a number of observational studies, including most recently the superposed epoch analysis of Tetrick et al. (2017), which showed that EMIC wave onsets observed by the Van Allen Probes occurred on average within 2 hr of increases in Psw and/or AE. Drozdov et al. (2017) compared the effectiveness of parameterizing EMIC waves in the Versatile Electron Radiation Belt model using several geophysical variables and indices and found that using increased solar wind dynamic pressure provided a better agreement with observations of ultrarelativistic radiation belt fluxes and local minima in phase space density profiles than using other variables (K_p , Dst, AE, and Vsw).

7. Conclusions

Although the primary purpose of this paper is to present EMIC observations during the GEM QARBM challenge intervals so that modelers can incorporate actual EMIC data rather than parameterized values in their models, we have also compared this EMIC data set to relativistic and ultrarelativistic electron data from the Van Allen Probes. These comparisons revealed two examples of depletions of ultrarelativistic electrons consistent with all of the accepted predictions of the effects of EMIC waves: depletions in phase space densities and pitch angle distributions more narrowly peaked near 90° that were localized in L^* to the same regions where the waves were observed. These characteristics were typically observed most clearly between $L^* = 3.5$ and 4.5^* . Although observed depletions up to even $L^* = 6$ are consistent with the EMIC wave observations presented here, it becomes increasingly difficult to exclude the effects of outward radial diffusion at these higher L^* values. Other EMIC events, with ostensibly similar wave amplitude, had more short-lived impacts or even no impact on ultrarelativistic electron distributions. The fact that non-adiabatic loss of electrons did not occur in every case during which strong or even intense EMIC waves were observed highlights the need for multipoint observations and careful analysis in order to provide sufficient evidence to delineate between dominant source, transport, and loss processes in the Earth's radiation belts.

This study has also demonstrated that the combination of wave data from equatorially orbiting satellites and ground-based search coil magnetometers, along with POES proton precipitation data, gives a significantly more complete picture of EMIC wave occurrence in the region of the outer radiation belt than that available from in situ spacecraft observations alone. However, because of the limitations in local time and L shell coverage of ground-based induction magnetometers and POES spacecraft, the available data may still provide a less than complete picture of EMIC wave activity during the four GEM QARBM challenge intervals. The longitudinal coverage of ground-based induction magnetometers has been significantly augmented since 2013, most notably thanks to efforts by the PWING/ARASE group at Nagoya University (Shiokawa et al., 2017) and the addition of three U.S. instruments in Antarctica (2) and Canada, so studies of radiation belt enhancements and depletions occurring more recently may benefit from considerably more complete coverage. However, obtaining spatially complete data with accurate, calibrated amplitude information on EMIC wave activity in the radiation belts is likely to remain elusive because of the spatially limited nature of many EMIC events,

the currently limited number of in situ and POES spacecraft, and the absence of latitudinally spaced ground-based induction magnetometers in most longitude sectors.

Acknowledgments

We thank the referees for their helpful comments and corrections. We acknowledge the GEM *Quantitative Assessment of Radiation Belt Modeling* focus group for motivating this study. We thank David Sibeck and Kjellmar Oksavik for helpful comments, and Viacheslav Pilipenko for his assistance in obtaining the induction coil data from Russian observatories. Work at Augsburg University was supported by National Science Foundation grants PLR-1341493, AGS-1264146, and AGS-1651263, and work performed by M. J. E. at NASA/GSFC was supported by the Van Allen Probes mission. W. L. acknowledges support from NSF grant AGS-1723588, AFOSR grant FA9550-15-1-0158, and the Alfred P. Sloan Research Fellowship FG-2018-10936. Work performed by Q. M. was supported by the Van Allen Probes Mission via JHU/APL contracts 967399 and 921647. A. C. K. acknowledges support from NASA grant NNS16AG78G and NSF grant AGS-1552321. M. R. L. acknowledges support from NSF grant PLR-1341677. Research at the British Antarctic Survey was supported by the Natural Environment Research Council (NERC) Highlight Topic Grant NE/P01738X/1 (Rad/Sat) and National Capability funding grant NE/R016038/1. The authors thank I. R. Mann, D. K. Milling, and the rest of the CARISMA team for data. CARISMA is operated by the University of Alberta, funded by the Canadian Space Agency. The operation of STEL magnetometers at Magadan and Paratunka is made in collaboration with the Institute of Cosmophysical Researches and Radio Wave Propagation (IKIR), Far-Eastern Branch of the Russian Academy of Sciences. The operation at Athabasca is made in collaboration with the Athabasca University. K. S. is supported by JSPS KAKENHI 15H05815 and 16H06286. E. E. acknowledges support from Russian Foundation for Basic Research grant 18-05-00108. Van Allen Probes research at the University of Colorado, the University of Iowa, the University of Minnesota, the University of New Hampshire, UCLA, and the Aerospace Corporation was supported by NASA prime contract NASS-01072 to The Johns Hopkins University Applied Physics Laboratory. We gratefully acknowledge use of NASA/GSFC's Space Physics Data Facility's OMNIWeb, SSCweb, and CDASWeb data. Van Allen Probes CDF data files are available at <http://www.space.umn.edu/rbspewf-wdata/> and <http://rbsp.space.umn.edu/rbspdata/> (EFW), <http://emfisis.physics.uiowa.edu/data/index> (EMFISIS), and <https://www.rbsp-ect.lanl.gov/science/DataDirectories.php> (REPT and MagEIS).

References

Anderson, B. J., Erlandson, R. E., & Zanetti, L. J. (1992). A statistical study of Pc 1-2 magnetic pulsations in the equatorial magnetosphere. 1. Equatorial occurrence distributions. *Journal of Geophysical Research*, *97*(A3), 3075–3088. <https://doi.org/10.1029/91JA02706>

Angelopoulos, V. (2008). The THEMIS mission. *Space Science Reviews*, *141*(1–4), 5–34. <https://doi.org/10.1007/s11214-008-9336-1>

Aseev, N. A., Shprits, Y. Y., Drozdov, A. Y., Kellerman, A. C., Usanova, M. E., Wang, D., & Zhelavskaya, I. S. (2017). Signatures of ultrarelativistic electron loss in the heart of the outer radiation belt measured by Van Allen Probes. *Journal of Geophysical Research: Space Physics*, *122*, 10,102–10,111. <https://doi.org/10.1002/2017JA024485>

Baker, D. N., Jaynes, A. N., Li, X., Henderson, M. G., Kanekal, S. G., Reeves, G. D., et al. (2014). Gradual diffusion and punctuated phase space density enhancements of highly relativistic electrons: Van Allen Probes observations. *Geophysical Research Letters*, *41*, 1351–1358. <https://doi.org/10.1002/2013GL058942>

Baker, D. N., Kanekal, S. G., Hoxie, V. C., Batiste, S., Bolton, M., Li, X., et al. (2013). The Relativistic Electron-Proton Telescope (REPT) instrument on board the Radiation Belt Storm Probes (RBSP) Spacecraft: Characterization of Earth's radiation belt high-energy particle populations. *Space Science Reviews*, *179*(1–4), 337–381. <https://doi.org/10.1007/s11214-012-9950-9>

Blake, J. B., Carranza, P. A., Claudepierre, S. G., Clemmons, J. H., Crain, W. R., Dotan, Y., et al. (2013). The magnetic electron ion spectrometer (MagEIS) instruments aboard the Radiation Belt Storm Probes (RBSP) spacecraft. *Space Science Reviews*, *179*, 383–421. <https://doi.org/10.1007/s11214-013-9991-8>

Boyd, A. J. (2016). Quantifying the role of the seed population in radiation belt dynamics (Pembroke, Ont.), Ph. D. thesis, University of New Hampshire, Durham, NH.

Boynton, R. J., Mourenas, D., & Balikhin, M. A. (2017). Electron flux dropouts at $L = 4.2$ from Global Positioning System satellites: Occurrences, magnitudes, and main driving factors. *Journal of Geophysical Research: Space Physics*, *122*, 11,428–11,441. <https://doi.org/10.1002/2017JA024523>

Carson, B. R., Rodger, C. J., & Clilverd, M. A. (2013). POES satellite observations of EMIC-wave driven relativistic electron precipitation during 1998–2010. *Journal of Geophysical Research: Space Physics*, *118*, 232–243. <https://doi.org/10.1029/2012JA017998>

Drozdov, A. Y., Shprits, Y. Y., Usanova, M. E., Aseev, N. A., Kellerman, A. C., & Zhu, H. (2017). EMIC wave parameterization in the long-term VERB code simulation. *Journal of Geophysical Research: Space Physics*, *122*, 8488–8501. <https://doi.org/10.1002/2017JA024389>

Engebretson, M. J., Lessard, M. R., Bortnik, J., Green, J. C., Horne, R. B., Detrick, D. L., et al. (2008). Pc1-Pc2 waves and energetic particle precipitation during and after magnetic storms: Superposed epoch analysis and case studies. *Journal of Geophysical Research*, *113*, A01211. <https://doi.org/10.1029/2007JA012362>

Engebretson, M. J., Peterson, W. K., Posch, J. L., Klatt, M. R., Anderson, B. J., Russell, C. T., et al. (2002). Observations of two types of Pc 1-2 pulsations in the outer dayside magnetosphere. *Journal of Geophysical Research*, *107*(A12), 1451. <https://doi.org/10.1029/2001JA000198>

Engebretson, M. J., Posch, J. L., Westerman, A. M., Otto, N. J., Slavin, J. A., Le, G., et al. (2008). Temporal and spatial characteristics of Pc 1 waves observed by ST5. *Journal of Geophysical Research*, *113*, A07206. <https://doi.org/10.1029/2008JA013145>

Engebretson, M. J., Posch, J. L., Wygant, J. R., Kletzing, C. A., Lessard, M. R., Huang, C.-L., et al. (2015). Van Allen probes, NOAA, GOES, and ground observations of an intense EMIC wave event extending over 12 h in magnetic local time. *Journal of Geophysical Research: Space Physics*, *120*, 5465–5488. <https://doi.org/10.1002/2015JA021227>

Erlandson, R. E., Zanetti, L. J., Potemra, T. A., Block, L. P., & Holmgren, G. (1990). Viking magnetic and electric field observations of Pc 1 waves at high latitudes. *Journal of Geophysical Research*, *95*(A5), 5941–5955. <https://doi.org/10.1029/JA095iA05p05941>

Evans, D. S., & Greer, M. S. (2004). Polar Orbiting Environmental Satellite Space Environment Monitor-2: Instrument descriptions and archive data documentation. NOAA Tech. Mem. 93, Version 1.4. Space Weather Predict. Cent., Boulder, Colo.

Fok, M. C., Glocer, A., Zheng, Q., Horne, R. B., Meredith, N. P., Albert, J. M., & Nagai, T. (2011). Recent developments in the radiation belt environment model. *Journal of Atmospheric and Solar: Terrestrial Physics*, *73*(11–12), 1435–1443. <https://doi.org/10.1016/j.jastp.2010.09.033>

Forsyth, C., Rae, I. J., Murphy, K. R., Freeman, M. P., Huang, C.-L., Spence, H. E., et al. (2016). What effect do substorms have on the content of the radiation belts? *Journal of Geophysical Research: Space Physics*, *121*, 6292–6306. <https://doi.org/10.1002/2016JA022620>

Foster, J. C., Erickson, P. J., Baker, D. N., Claudepierre, S. G., Kletzing, C. A., Kurth, W., et al. (2014). Prompt energization of relativistic and highly relativistic electrons during a substorm interval: Van Allen Probes observations. *Geophysical Research Letters*, *41*, 20–25. <https://doi.org/10.1002/2013GL058438>

Fraser, B. J. (1975). Ionospheric duct propagation and Pc1 source regions. *Journal of Geophysical Research*, *80*(19), 2790–2796. <https://doi.org/10.1029/JA080i019p02790>

Fujita, S. (1988). Duct propagation of hydromagnetic waves in the upper ionosphere: II. Dispersion characteristics and loss mechanism. *Journal of Geophysical Research*, *93*(A12), 14,674–14,682. <https://doi.org/10.1029/JA093iA12p14674>

Fujita, S., & Tamao, T. (1988). Duct propagation of hydromagnetic waves in the upper ionosphere, 1, electromagnetic field distributions in high latitudes associated with localized incidence of a shear Alfvén wave. *Journal of Geophysical Research*, *93*(A12), 14,665–14,673. <https://doi.org/10.1029/JA093iA12p14665>

Glauert, S. A., Horne, R. B., & Meredith, N. P. (2014). Three-dimensional electron radiation belt simulations using the BAS Radiation Belt Model with new diffusion models for chorus, plasmaspheric hiss, and lightning-generated whistlers. *Journal of Geophysical Research: Space Physics*, *119*, 268–289. <https://doi.org/10.1002/2013JA019281>

Greifinger, C., & Greifinger, P. (1968). Theory of hydromagnetic propagation in the ionosphere wave guide. *Journal of Geophysical Research*, *73*(23), 7473–7490. <https://doi.org/10.1029/JA073i023p07473>

Greifinger, C., & Greifinger, P. (1973). Wave guide propagation of micropulsations out of the plane of the geomagnetic meridian. *Journal of Geophysical Research*, *78*(22), 4611–4618. <https://doi.org/10.1029/JA078i022p04611>

Horne, R. B., & Thorne, R. M. (1993). On the preferred source location for the convective amplification of ion cyclotron waves. *Journal of Geophysical Research*, *98*(A6), 9233–9247. <https://doi.org/10.1029/92JA02972>

Iyemori, T., & Hayashi, K. (1989). Pc 1 micropulsations observed by Magsat in the ionospheric F region. *Journal of Geophysical Research*, *94*(A1), 93–100. <https://doi.org/10.1029/JA094iA01p0093>

Kang, S.-B., Fok, M.-C., Komar, C., Glocer, A., Li, W., & Buzulukova, N. (2018). An energetic electron flux dropout due to magnetopause shadowing on 1 June 2013. *Journal of Geophysical Research: Space Physics*, *123*, 1178–1190. <https://doi.org/10.1002/2017JA024879>

PSD and adiabatic invariant computations were made using code developed by A. C. K., the IRBEM library, and the UCLA Hoffman2 cluster. Data files can be made available by request to A. C. K. GOES magnetometer data are archived at NOAA's National Centers for Environmental Information (NCEI) http://satdat.ngdc.noaa.gov/sem/goes/data/new_full/. THEMIS magnetic field spectrograms and data are available at http://themis.ssl.berkeley.edu/overview_data.shtml. POES data can be accessed at <https://cdaweb.sci.gsfc.nasa.gov>. Spectrograms from search coil magnetometers at Halley Station (operated by the British Antarctic Survey) and South Pole Station (operated by the U.S. Antarctic Program) can be accessed at <http://space.augsburg.edu/searchcoil/index.html>. CARISMA induction coil magnetometer data and spectrograms can be accessed at <http://carisma.ca/>. STEL induction magnetometer spectrograms can be accessed at <http://stdb2.stelab.nagoya-u.ac.jp/magne/>. Finnish chain pulsation magnetometer spectrograms can be accessed at <http://www.sgo.fi/Data/Pulsation/pulArchive.php>. Data from Russian stations can be provided by the respective coauthors: Borok data from Eldar Dmitriev, Nizhny Novgorod data from Elena Ermakova, and Uzur data from Ravil Rakhmatulin.

- Kersten, T., Horne, R. B., Glauert, S. A., Meredith, N. P., Fraser, B. J., & Grew, R. S. (2014). Electron losses from the radiation belts caused by EMIC waves. *Journal of Geophysical Research: Space Physics*, *119*, 8820–8837. <https://doi.org/10.1002/2014JA020366>
- Kim, H., Lessard, M. R., Engebretson, M. J., & Luhr, H. (2010). Ducting characteristics of Pc 1 waves at high latitudes on the ground and in space. *Journal of Geophysical Research*, *115*, A09310. <https://doi.org/10.1029/2010JA015323>
- Kim, H., Lessard, M. R., Engebretson, M. J., & Young, M. A. (2011). Statistical study of Pc1-2 wave propagation characteristics in the high-latitude ionospheric waveguide. *Journal of Geophysical Research*, *116*, A07227. <https://doi.org/10.1029/2010JA016355>
- Kletzing, C. A., Kurth, W. S., Acuna, M., MacDowall, R. J., Torbert, R. B., Averkamp, T., et al. (2013). The Electric and Magnetic Field Instrument Suite and Integrated Science (EMFISIS) on RBSP. *Space Science Reviews*, *179*(1–4), 127–181. <https://doi.org/10.1007/s11214-013-9993-6>
- Li, W., Ni, B., Thorne, R. M., Bortnik, J., Green, J. C., Kletzing, C. A., et al. (2013). Constructing the global distribution of chorus wave intensity using measurements of electrons by the POES satellites and waves by the Van Allen Probes. *Geophysical Research Letters*, *40*, 4526–4532. <https://doi.org/10.1002/grl.50920>
- Li, W., Thorne, R. M., Ma, Q., Ni, B., Bortnik, J., Baker, D. N., et al. (2014). Radiation belt electron acceleration by chorus waves during the 17 March 2013 storm. *Journal of Geophysical Research: Space Physics*, *119*, 4681–4693. <https://doi.org/10.1002/2014JA019945>
- Li, Z., Hudson, M. K., Jaynes, A. N., Boyd, A. J., Malaspina, D. M., Thaller, S. A., et al. (2014). Modeling gradual diffusion changes in radiation belt electron phase space density for the March 2013 Van Allen Probes case study. *Journal of Geophysical Research: Space Physics*, *119*, 8396–8403. <https://doi.org/10.1002/2014JA020359>
- Lundblad, J. A., & Soraas, F. (1978). Proton observations supporting the ion cyclotron wave heating theory of SAR arc formation. *Planetary and Space Science*, *26*(3), 245–254. [https://doi.org/10.1016/0032-0633\(78\)90090-9](https://doi.org/10.1016/0032-0633(78)90090-9)
- Ma, Q., Li, W., Bortnik, J., Thorne, R. M., Chu, X., Ozeke, L. G., et al. (2018). Quantitative evaluation of radial diffusion and local acceleration processes during GEM challenge events. *Journal of Geophysical Research: Space Physics*, *123*, 1938–1952. <https://doi.org/10.1002/2017JA025114>
- Mann, I. R., Milling, D. K., Rae, I. J., Ozeke, L. G., Kale, A., Kale, Z. C., et al. (2008). The upgraded CARISMA magnetometer array in the THEMIS era. *Space Science Reviews*, *141*(1–4), 413–451. <https://doi.org/10.1007/s11214-008-9457-6>
- Mauk, B. H., Fox, N. J., Kanekal, S. G., Kessel, R. L., Sibeck, D. G., & Ukhorskiy, A. (2013). Science objectives and rationale for the Radiation Belt Storm Probes Mission. *Space Science Reviews*, *179*(1–4), 3–27. <https://doi.org/10.1007/s11214-012-9908-y>
- Meredith, N. P., Thorne, R. M., Horne, R. B., Summers, D., Fraser, B. J., & Anderson, R. R. (2003). Statistical analysis of relativistic electron energies for cyclotron resonance with EMIC waves observed on CRRES. *Journal of Geophysical Research*, *108*(A6), 1250. <https://doi.org/10.1029/2002JA009700>
- Mourenas, D., Artemyev, A. V., Ma, Q., Agapitov, O. V., & Li, W. (2016). Fast dropouts of multi-MeV electrons due to combined effects of EMIC and whistler mode waves. *Geophysical Research Letters*, *43*, 4155–4163. <https://doi.org/10.1002/2016GL068921>
- Ni, B., Cao, X., Zou, Z., Zhou, C., Gu, X., Bortnik, J., et al. (2015). Resonant scattering of outer zone relativistic electrons by multiband EMIC waves and resultant electron loss time scales. *Journal of Geophysical Research: Space Physics*, *120*, 7357–7373. <https://doi.org/10.1002/2015JA021466>
- Ni, B., Li, W., Thorne, R. M., Bortnik, J., Green, J. C., Kletzing, C. A., et al. (2014). A novel technique to construct the global distribution of whistler mode chorus wave intensity using low-altitude POES electron data. *Journal of Geophysical Research: Space Physics*, *119*, 5685–5699. <https://doi.org/10.1002/2014JA019935>
- Ødegaard, L.-K. G., Tyssøy, H. N., Sandanger, M. I. J., Stadsnes, J., & Soraas, F. (2016). Space weather impact on the degradation of NOAA POES MEPED proton detectors. *Journal of Space Weather and Space Climate*, *6*, A26. <https://doi.org/10.1051/swsc/2016020>
- Sandanger, M., Soraas, F., Aarsnes, K., Oksavik, K., & Evans, D. S. (2007). Loss of relativistic electrons: Evidence for pitch angle scattering by electromagnetic ion cyclotron waves excited by unstable ring current protons. *Journal of Geophysical Research*, *112*, A12213. <https://doi.org/10.1029/2006JA012138>
- Sandanger, M. I., Ødegaard, L.-K. G., Nesse Tyssøy, H., Stadsnes, J., Soraas, F., Oksavik, K., & Aarsnes, K. (2015). In-flight calibration of NOAA POES proton detectors—Derivation of the MEPED correction factors. *Journal of Geophysical Research: Space Physics*, *120*, 9578–9593. <https://doi.org/10.1002/2015JA021388>
- Shiokawa, K., Katoh, Y., Hamaguchi, Y., Yamamoto, Y., Adachi, T., Ozaki, M., et al. (2017). Ground-based instruments of the PWING project to investigate dynamics of the inner magnetosphere at subauroral latitudes as a part of the ERG-ground coordinated observation network. *Earth, Planets and Space*, *69*(1), 160. <https://doi.org/10.1186/s40623-017-0745-9>
- Shprits, Y. Y., Drozdov, A. Y., Spasojevic, M., Kellerman, A. C., Usanova, M. E., Engebretson, M. J., et al. (2016). Wave-induced loss of ultra-relativistic electrons in the Van Allen radiation belts. *Nature Communications*, *7*, 12883. <https://doi.org/10.1038/ncomms12883>
- Shprits, Y. Y., Kellerman, A. C., Drozdov, A. Y., Spence, H. E., Reeves, G. D., & Baker, D. N. (2015). Combined convective and diffusive simulations: VERB-4D comparison with 17 March 2013 Van Allen Probes observations. *Geophysical Research Letters*, *42*, 9600–9608. <https://doi.org/10.1002/2015GL065230>
- Singer, H. J., Matheson, L., Grubb, R., Newman, A., & Bower, S. D. (1996). Monitoring space weather with the GOES magnetometers. In E. R. Washwell (Ed.), *SPIE Conference Proceedings* (Vol. 2812, pp. 299–308). Bellingham, Wash: GOES-8 and Beyond SPIE.
- Soraas, F., Lundblad, J. A., Maltseva, N. F., Troitskaya, V., & Selivanov, V. (1980). A comparison between simultaneous I.P.D.P. groundbased observations and observations of energetic protons obtained by satellites. *Planetary and Space Science*, *28*(4), 387–405. [https://doi.org/10.1016/0032-0633\(80\)90043-4](https://doi.org/10.1016/0032-0633(80)90043-4)
- Spence, H. E., Reeves, G. D., Baker, D. N., Blake, J. B., Bolton, M., Bourdarie, S., et al. (2013). Science goals and overview of the Energetic Particle, Composition, and Thermal Plasma (ECT) suite on NASA's Radiation Belt Storm Probes (RBSP) Mission. *Space Science Reviews*, *179*, 311–336. <https://doi.org/10.1007/s11214-013-0007-5>
- Su, Z., Gao, Z., Zhu, H., Li, W., Zheng, H., Wang, Y., et al. (2016). Nonstorm time dropout of radiation belt electron fluxes on 24 September 2013. *Journal of Geophysical Research: Space Physics*, *121*, 6400–6416. <https://doi.org/10.1002/2016JA022546>
- Summers, D., Shi, R., Engebretson, M. J., Oksavik, K., Manweiler, J. W., & Mitchell, D. G. (2017). Energetic proton spectra measured by the Van Allen Probes. *Journal of Geophysical Research: Space Physics*, *122*, 10,129–10,144. <https://doi.org/10.1002/2017JA024484>
- Summers, D., & Thorne, R. M. (2003). Relativistic electron pitch-angle scattering by electromagnetic ion cyclotron waves during geomagnetic storms. *Journal of Geophysical Research*, *108*(A4), 1143. <https://doi.org/10.1029/2002JA009489>
- Takahashi, K., Anderson, B. J., & Strangeway, R. J. (1990). AMPTE CCE observations of pc 3–4 pulsations at L = 2–6. *Journal of Geophysical Research*, *95*, 17,179–17,186.
- Tetrick, S. S., Engebretson, M. J., Posch, J. L., Olson, C. N., Smith, C. W., Denton, R. E., et al. (2017). Location of intense electromagnetic ion cyclotron (EMIC) wave events relative to the plasmopause: Van Allen Probes observations. *Journal of Geophysical Research: Space Physics*, *122*, 4064–4088. <https://doi.org/10.1002/2016JA023392>

- Tsyganenko, N. A. (1989). A magnetospheric magnetic field model with a warped tail current sheet. *Planetary and Space Science*, 37(1), 5–20. [https://doi.org/10.1016/0032-0633\(89\)90066-4](https://doi.org/10.1016/0032-0633(89)90066-4)
- Tsyganenko, N. A., & Sitnov, M. I. (2005). Modeling the dynamics of the inner magnetosphere during strong geomagnetic storms. *Journal of Geophysical Research*, 110, A03208. <https://doi.org/10.1029/2004JA010798>
- Tsyganenko, N. A., & Sitnov, M. I. (2007). Magnetospheric configurations from a high-resolution data-based magnetic field model. *Journal of Geophysical Research*, 112, A06225. <https://doi.org/10.1029/2007JA012260>
- Ukhorskiy, A. Y., Sitnov, M. I., Millan, R. M., Kress, B. T., Fennell, J. F., Claudepierre, S. G., & Barnes, R. J. (2015). Global storm time depletion of the outer electron belt. *Journal of Geophysical Research: Space Physics*, 120, 2543–2556. <https://doi.org/10.1002/2014JA020645>
- Usanova, M. E., Drozdov, A., Orlova, K., Mann, I. R., Shprits, Y., Robertson, M. T., et al. (2014). Effect of EMIC waves on relativistic and ultrarelativistic electron populations: Ground-based and Van Allen Probes observations. *Geophysical Research Letters*, 41, 1375–1381. <https://doi.org/10.1002/2013GL059024>
- Usanova, M. E., Mann, I. R., Bortnik, J., Shao, L., & Angelopoulos, V. (2012). THEMIS observations of electromagnetic ion cyclotron wave occurrence: Dependence on AE, SYMH, and solar wind dynamic pressure. *Journal of Geophysical Research*, 117, A10218. <https://doi.org/10.1029/2012JA018049>
- Wang, C., Ma, Q., Tao, X., Zhang, Y., Teng, S., Albert, J. M., et al. (2017). Modeling radiation belt dynamics using a 3D layer method code. *Journal of Geophysical Research: Space Physics*, 122, 8642–8658. <https://doi.org/10.1002/2017JA024143>
- Wygant, J. R., Bonnell, J. W., Goetz, K., Ergun, R. E., Mozer, F. S., Bale, S. D., et al. (2013). The electric field and waves instruments on the Radiation Belt Storm Probes mission. *Space Science Reviews*, 179(1–4), 183–220. <https://doi.org/10.1007/s11214-013-0013-7>
- Xiang, Z., Tu, W., Li, X., Ni, B., Morley, S. K., & Baker, D. N. (2017). Understanding the mechanisms of radiation belt dropouts observed by Van Allen Probes. *Journal of Geophysical Research: Space Physics*, 122, 9858–9879. <https://doi.org/10.1002/2017JA024487>
- Xiao, F., Yang, C., He, Z., Su, Z., Zhou, Q., He, Y., et al. (2014). Chorus acceleration of radiation belt relativistic electrons during March 2013 geomagnetic storm. *Journal of Geophysical Research: Space Physics*, 119, 3325–3332. <https://doi.org/10.1002/2014JA019822>
- Yahnin, A. G., & Yahnina, T. A. (2007). Energetic proton precipitation related to ion-cyclotron waves. *Journal of Atmospheric and Solar Terrestrial Physics*, 69(14), 1690–1706. <https://doi.org/10.1016/j.jastp.2007.02.010>
- Yahnin, T. A., Yahnin, A. G., Kangas, J., & Manninen, J. (2000). Proton precipitation related to Pc1 pulsations. *Geophysical Research Letters*, 27(21), 3575–3578. <https://doi.org/10.1029/2000GL003763>
- Zhang, X.-J., Li, W., Thorne, R. M., Angelopoulos, V., Ma, Q., Li, J., et al. (2016). Physical mechanism causing rapid changes in ultrarelativistic electron pitch angle distributions right after a shock arrival: Evaluation of an electron dropout event. *Journal of Geophysical Research: Space Physics*, 121, 8300–8316. <https://doi.org/10.1002/2016JA022517>
- Zhang, X.-J., Mourenas, D., Artemyev, A. V., Angelopoulos, V., & Thorne, R. M. (2017). Contemporaneous EMIC and whistler mode waves: Observations and consequences for MeV electron loss. *Geophysical Research Letters*, 44, 8113–8121. <https://doi.org/10.1002/2017GL03886>
- Zhang, X.-J., Tu, W., Li, X., Ni, B., Morley, S. K., & Baker, D. N. (2016). Direct evidence for EMIC wave scattering of relativistic electrons in space. *Journal of Geophysical Research: Space Physics*, 121, 6620–6631. <https://doi.org/10.1002/2016JA022521>
- Zhang, Y., Shi, R., Ni, B., Gu, X., Zhang, X., Zuo, P., et al. (2017). Inferring electromagnetic ion cyclotron wave intensity from low altitude POES proton flux measurements: A detailed case study with conjugate Van Allen Probes observations. *Advances in Space Research*, 59(6), 1568–1576. <https://doi.org/10.1016/j.asr.2016.12.035>